https://doi.org/10.5194/egusphere-2026-3060
Preprint. Discussion started: 10 July 2026

Linking open-ocean polynyas and deep convection in the Southern Ocean across CMIP6 models

Shunzi Lu[1], Irina Marinov[1], and Sergey Molodtsov[1,2]

[1]Department of Earth and Environmental Science, University of Pennsylvania, Philadelphia, PA 19104, USA
[2]International Arctic Research Center, University of Alaska Fairbanks, Fairbanks, 99775, USA

Correspondence: Shunzi Lu (shunzlu@sas.upenn.edu)

Abstract. Open-ocean polynyas (OOPs) and deep convection in the Southern Ocean are critical features of the global climate system, however, their representation and mutual dependence in climate models remain poorly understood. This study investigates the occurrence and coupling of OOPs and deep convection across 49 CMIP6 models using long-term pre-industrial control simulations. Our results reveal that while most models simulate both phenomena, their spatial and temporal co-occurrence varies substantially. Although deep convection is typically associated with surface salinification and heat loss, it does not always result in detectable polynyas. We identify two distinct regimes of OOPs across the ensemble: "deep OOPs", which are directly coupled to deep ocean convection, and "shallow OOPs", which form independently of deep mixing, likely driven by surface forcing or sea-ice divergence. The representation of these regimes is strongly influenced by the choice of ocean model component. These findings highlight the importance of process-based diagnostics in evaluating Southern Ocean overturning and suggest that the connection between surface polynyas and deep water formation is more complex than traditionally assumed in climate models.

1 Introduction

Polynyas are ice-enclosed regions of nearly open water that occur in high-latitude oceans. As sea ice forms and thickens during the cold months in each hemisphere, it acts as an insulating barrier between the ocean and the atmosphere, thereby influencing regional thermodynamics and air-sea gas exchange. The presence of large polynyas in wintertime enables substantial heat and gas transfer from the ocean to the atmosphere, which can significantly impact atmospheric dynamics and the global heat and carbon budget (Fusco et al., 2009; Bernardello et al., 2014; Cabré et al., 2017; Weijer et al., 2017; Kaufman et al., 2020).

In the Southern Ocean (SO), polynyas occasionally occur within the sea-ice zone surrounding the Antarctic ice sheet (Barber and Massom, 2007). Most polynyas are typically found near the Antarctic shelf and are known as coastal polynyas. Their formation is primarily driven by strong katabatic winds and divergent ocean currents that displace freshly formed sea ice away from the Antarctic continent (Bromwich and Kurtz, 1984; Thompson et al., 2020). Coastal polynyas facilitate significant heat loss from the ocean through latent heat of fusion, and are thus considered as latent heat polynyas. As a result, they are key sites for intense sea ice production and the associated salinization of shelf water, processes that contribute substantially to the Antarctic Bottom Water (AABW) formation (Morales Maqueda et al., 2004; Tamura et al., 2008; Ohshima et al., 2013, 2016).

https://doi.org/10.5194/egusphere-2026-3060
Preprint. Discussion started: 10 July 2026

In contrast, open-ocean polynyas (OOPs), first observed in the Weddell Sea via satellite microwave radiometry in the 1970s (Carsey, 1980; Comiso and Gordon, 1987), form within the interior of the sea ice pack over the deep ocean. OOPs are thought to be thermally driven and maintained by deep-reaching convection, which induces heat into the surface layer (Gordon, 1982). The convective upwelling of warm Circumpolar Deep Water (CDW) supplies sufficient energy to melt the overlying sea ice and suppress the formation of new ice (Holland, 2001; Cheon et al., 2014; Cheon and Gordon, 2019). Thus, they are also referred to as sensible heat polynyas, which have lower ice production rates compared to coastal polynyas, and are likely to be found in areas with enhanced oceanic heat flux, such as tidal straits or near seamounts (Morales Maqueda et al., 2004).

Several mechanisms have been proposed to explain the initiation of large OOP. A number of studies have emphasized the role of topographically induced ocean dynamics, wherein mesoscale eddies generated by flow over seamounts can induce sea-ice divergence via anomalies in Ekman stress, thereby creating ice-free regions (Holland, 2001). These eddies can also uplift isopycnals and weaken the stratification, thereby preconditioning the water column for deep convection (de Steur et al., 2007). Atmospheric forcing has also been identified as a key triggering mechanism. Parkinson (1983) simulated the formation of the Weddell polynya through the encirclement of an open-water region by sea ice under conditions of low atmospheric pressure. Intense polar cyclones or storms can similarly drive pronounced sea-ice divergence and expose the ocean surface to rapid heat loss, enabling the onset of localized convection (Francis et al., 2019). However, Tesdal et al. (2023) argued that even when surface forcing is sufficiently strong to drive local convection, these processes alone may not fully destabilize the upper ocean; the interior mixing regime and the background stratification critically determine whether such perturbations can actually induce overturning to abyssal depths. More recent work by Narayanan et al. (2024) identified an Ekman-driven lateral salt transport mechanism: enhanced easterly winds generate cross-frontal Ekman flow that advects saline water across a surface jet near Maud Rise, thereby increasing surface salinity and promoting buoyancy instability. This process facilitates vertical mixing and helps counteract the stabilizing influence of freshwater input, providing a quantitative pathway by which the system can be tipped into a deep-convection regime. A recent study of the Cosmonaut Sea polynya further demonstrated that its formation and variability are governed by a complex interplay among atmospheric, oceanic, and climatic processes operating over multiple timescales (Dutta et al., 2026).

Some polynyas recur consistently at fixed geographic locations, likely influenced by underlying bottom topography (Morales Maqueda et al., 2004). A notable example is the Weddell Polynya near Maud Rise, which persisted throughout the austral winters of 1974, 1975, and 1976 (Gordon et al., 2007; Zhou et al., 2026), and reappeared in the Weddell Sea during 2016 and 2017 (Campbell et al., 2019; Jena et al., 2019). Similarly, an exceptionally deep convective event occurred near Maud Rise in the 1970s, potentially reaching depths of 4,000 m (Gordon, 1978), with similar events possibly occurring in 2016 and 2017 (Cheon and Gordon, 2019).

The limited duration of satellite observations constrains long-term analysis of deep convection and OOPs. In contrast, numerical models can simulate ocean dynamics over centuries, capturing potential recurring cycles of deep convection and polynya events and their links to large-scale climate variability. For example, repeat cycles of deep convection and OOP on multi-decadal to multi-centennial timescales have been demonstrated in box models (Martin et al., 2013; Boot et al., 2021), ocean

https://doi.org/10.5194/egusphere-2026-3060
Preprint. Discussion started: 10 July 2026

general circulation models (Cheon et al., 2015; Kurtakoti et al., 2018), and coupled climate models (Goosse and Fichefet, 2001; Martin et al., 2013; Weijer et al., 2017; Huot et al., 2021; Rheinlænder et al., 2021; Diao et al., 2022).

Climate models participating in Phase 6 of the Coupled Model Intercomparison Project (CMIP6) show considerable variability in their simulations of SO sea ice (Roach et al., 2020; Li et al., 2021; Casagrande et al., 2023; Nie et al., 2023). This variability can directly influence the models' ability to represent key coupled processes such as OOP and deep convection events, which depend sensitively on sea-ice cover and its seasonal dynamics. Previous studies on earlier model generations and CMIP6 models have demonstrated that some models simulate repeat cycles of deep convection and polynyas on multi-decadal to multi-centennial timescales (de Lavergne et al., 2014). Notable examples include models from the GFDL family (Bernardello et al., 2014; Zanowski et al., 2015; Cabré et al., 2017).

Observations indicate that AABW is primarily formed on the Antarctic continental shelf, particularly within coastal polynyas where intense sea-ice formation leads to brine rejection and the production of dense shelf water, which subsequently cascades down the continental slope (Ohshima et al., 2022; Silvano et al., 2023; Golledge et al., 2025). However, most models participating in CMIP struggle to simulate these processes accurately, and often generate AABW through open-ocean deep convection within OOPs (Heuzé et al., 2013; Beadling et al., 2020; Jeong et al., 2020; Heuzé, 2021; Mohrmann et al., 2021). The coarse resolution of these models limits their ability to represent key dynamics and fine-scale bathymetry, while many models also show poor representation of ice-ocean interactions, including circulation beneath ice shelves and exchanges with the ice sheet (Asay-Davis et al., 2017; Seroussi et al., 2020).

Recent high-resolution models have improved the simulation of deep water formation on the Antarctic continental shelf (e.g., Li et al., 2023). Many CMIP6 models now show better representation of shelf water formation and coastal polynyas compared to earlier model generations (Mohrmann et al., 2021; Heuzé, 2021). However, OOPs remain prevalent in CMIP6 simulations and are often overrepresented relative to observations (Mohrmann et al., 2021). Moreover, increasing model resolution can, in some cases, enhance the occurrence of OOPs and deep convection (e.g., Diao et al., 2022; Jeong et al., 2023). These findings suggest that OOP formation and associated deep convection may be important to model behavior, and their underlying mechanisms require further investigation.

This study investigates naturally occurring deep convection and OOP events in the SO across 49 CMIP6 models using long-term pre-industrial control simulations. The central aim is to characterize the relationship between deep convection and OOPs under non-anthropogenic forcing conditions, and to identify the factors that favor their occurrence in certain models. Specifically, we address three questions: (i) how strongly OOPs and deep convection are coupled across the 49 models; (ii) whether models exhibit distinct regimes in which OOPs coincide with deep convection versus those characterized by shallow or absent convection; and (iii) which large-scale mean-state properties and model configurations favor each regime. To answer these questions, we apply a consistent detection framework to identify OOPs and convective events across models (Section 2), compare their spatial overlap and co-variability, and relate event statistics to SO stratification and surface forcing biases (Section 3). We further quantify the coupling between deep convection and OOPs and separate the different regimes (Section 4). We then synthesize behavior by ocean-model family (Section 5) to highlight structural dependencies. We conclude with a discussion of results and directions for future research.

https://doi.org/10.5194/egusphere-2026-3060
Preprint. Discussion started: 10 July 2026

2 Identifying deep convection and OOP events in CMIP6 models

The primary objective of this study is to explore deep convection and OOP events in the SO and their interconnections across CMIP6 models. To investigate the occurrences of deep convection events and OOPs across different models, it is essential to establish a standardized identification framework based on available diagnostic outputs. The diagnostic protocols provided by the Ocean Model Intercomparison Project (OMIP) and the Sea-Ice Model Intercomparison Project (SIMIP), both endorsed by CMIP6, offer guidelines for ocean and sea ice related variables to enable consistent cross-model analysis (Eyring et al., 2016; Griffies et al., 2016; Notz et al., 2016).

2.1 CMIP6 models

The identification of deep convection and OOP events in the SO requires integrating multiple indicators. However, not all models include the full set of necessary variables for public access. Therefore, only a subset of models is chosen for this study. We explore and expand existing methodologies for deep convection and OOP identification on the selected subset of CMIP6 models.

Within all standardized simulations designed to benchmark model behavior from CMIP6, we focus specifically on the pre-industrial control (piControl) simulations, which represent the long-term, stable quasi-equilibrium climate state in the absence of anthropogenic forcing, offering a reference for understanding natural variability in the interactions between ice, ocean, and atmosphere. A total of 49 models from 25 modeling centers were selected based on the availability of key diagnostic variables and a minimum simulation length of 300 years. For each model, we use the last 500 years of data when available; for those with shorter durations, the full length of the simulation is included. The majority of models provide data outputs for only one ensemble member, with the variant "r1i1p1f1" being the most commonly available. We prioritized the use of the variant "r1i1p1f1", and used alternative ensembles when this variant is unavailable. Given our focus on the large-scale OOPs that persist over multiple years, monthly mean data were sufficient for the analysis. We use area-weighted monthly averages of relevant oceanic and sea ice variables. Table 1 summarizes the selected models and relevant details. We separate models into different groups based on their ocean module used in each model to facilitate inter-model comparison.

Spatial resolution is also a key factor influencing the accuracy of models, as high-resolution models can capture small-scale convection processes better (e.g. Diao et al., 2022). All model outputs are analyzed on the original resolution of each model unless the outputs with the original grid are not accessible. Table 1 summarizes the horizontal and vertical resolutions of the models. For models with structured grids, the horizontal resolution refers to the number of data points in the meridional and zonal directions. For models with unstructured grids, the horizontal resolution corresponds to the total number of cells in the grid. The vertical resolution represents the number of vertical levels.

OOP and deep convection events occur predominantly during winter, while most CMIP6 models accurately capture the seasonal sea ice concentration (SIC) cycle, with maximum SIC typically observed in September (Beadling et al., 2020). Therefore, our analysis focuses on September mean model output for identifying OOP and deep convection events. Additionally, we

https://doi.org/10.5194/egusphere-2026-3060
Preprint. Discussion started: 10 July 2026

examine the climatological mean state of some seawater and sea ice properties for each model. For some of these properties, we also use data from all months to calculate annual means.

2.2 Identifying deep convection across models

The preconditioning for open-ocean deep convection occurs as a result of the interplay between water column destabilizing processes in the wintertime. On one hand, surface brine rejection and salinification lead to the formation of denser and heavier waters in the upper layers of the water column. On the other hand, subsurface advection of warmer waters disrupts the stratification of the deep water column. These processes collectively initiate convection, leading to water column mixing and the deepening of the mixed-layer depth (MLD). The identification and analysis of deep convection is therefore typically linked to MLD.

The selection of an MLD threshold to define deep convection varies depending on the specific research objectives and the regional oceanic characteristics. For example, studies have used critical depths of 700 m in the Nordic Seas and 1000 m in the Labrador Sea (e.g., Liu et al., 2024) to accommodate local bathymetric constraints. In contrast, in the deeper SO, de Lavergne et al. (2014) defined deep convection regions as MLD exceeding 2000 m and applied this across CMIP5 models. This definition has been widely adopted (e.g., Dufour et al., 2017; Chen et al., 2023). When identifying deep convection in the SO Atlantic sector in CMIP5 models, Reintges et al. (2017) applied an even higher September MLD threshold of 3000 m, while using a different MLD definition from that of de Lavergne et al. (2014). Beyond fixed MLD thresholds, alternative metrics have also been used. For example, ventilated volume, defined as the horizontal integral of MLDs greater than 500 m south of 60°S, has been used to analyze SO deep-reaching water properties in CMIP5 model (Behrens et al., 2016), showing similar categorization of convective and non-convective models to de Lavergne et al. (2014). Deep mixed volume, or mixed layer volume, which combines MLD and cell area, is another metric used to analyzed deep water properties and to assess deep convection in the SO (e.g., Heuzé, 2021; Zeller and Martin, 2024). Furthermore, Zhang et al. (2019) employed an AABW index as an indicator of deep convection strength in the SO.

Although alternative metrics provide detailed insights into deep water properties, an MLD-based method is sufficient for detecting deep convection in this study. Moreover, the variables required for this method are available for most models or can be readily derived from temperature and salinity fields when not directly provided. We use the September mean model output "mlotst", which represents the ocean mixed layer thickness defined by a density criterion, when provided by model directly. For models without this output, we calculate MLD from potential density following the method of de Boyer Montégut et al. (2004), i.e., the maximum depth at which the potential density differs from the surface (typically measured at 10 m depth) by less than 0.03 $\mathrm{kg/m^3}$. This density-based threshold method is commonly used to identify regions of substantial vertical mixing and is recommended by OMIP protocols (Griffies et al., 2016).

Potential density is derived from model diagnostic outputs seawater potential temperature ("thetao") and salinity ("so") using a TEOS-10 based seawater toolbox (see Appendix A for details). We apply this approach to all 49 models. In general, the calculated MLD matches well the model diagnostic variable "mlotst", though some discrepancies exist. In particular, for ACCESS-CM2, NorESM2-MM, NorESM2-LM, the calculated MLD in the Weddell and Ross Sea is shallower than the output

https://doi.org/10.5194/egusphere-2026-3060
Preprint. Discussion started: 10 July 2026

variable "mlotst" from the model; for CAS-ESM2-0 and FGOALS-g3, the calculated MLD is deeper in the SO than the "mlotst" from the model.

We examine different MLD threshold to detect deep convection in the GFDL-CM4 model as an example (Fig. 1a). Convection regions can shift locations from year to year over entire simulation period, therefore, we map all the locations where convection events can be detected after applying different thresholds. Both the locations and the size of the convection region vary depending on the threshold used. A relatively loose threshold of 1000 m categorizes most of the SO, including regions near Antarctic Circumpolar Current (ACC) band, as convective regions, which is not ideal for this study. In the contrast, A 2000 m threshold identifies convection primarily in the Weddell and Ross Sea, which is consistent with previous findings (de Lavergne et al., 2014).

We also analyze the standard deviation of MLD to identify regions with the greatest interannual variability. In the SO, MLD can be very shallow during non-convective periods and considerably deeper during convective periods, leading to large temporal fluctuations. Consequently, areas with frequent strong convection will show higher MLD variability than regions with less convection. Regions where the September MLD standard deviation exceeds the 97th percentile of all SO values are delineated by the black contour line in Fig. 1b. Using this criterion, we identify high-variability regions in both the Weddell and Ross Seas, consistent with convective areas detected using a 2000 m MLD threshold. In contrast, large areas near the ACC band that classified as convective based on a 1000 m threshold show lower MLD variability compared to the convective regions in the Weddell and Ross Sea, suggesting that the ACC maintains a persistently deep mixed layer, with limited multi-decadal variability. Therefore, applying a 1000 m threshold may capture regions lacking dynamic variability, thus obscuring detection of multi-decadal changes.

Our results highlight strong temporal variability in MLD in the Weddell and Ross Seas, indicative of periodic convection events. However, while the GFDL-CM4 model simulates a regular recurrence of deep convection events in the SO, this pattern may not be universal across climate models. The standard deviation-based method effectively identifies regions of pronounced and frequent convection but may underestimate the total convection area in models with weaker convection. Therefore, this approach may have limited applicability as a general convection detection method across different models.

We believe that in the SO, in order to have surface water mix with deep water, MLD should be more than 2000 m, as used in de Lavergne et al. (2014). Therefore, we use the MLD larger than 2000 m as criteria for detecting deep convection. Regions with MLD larger than 2000 m at least once in the entire analyzed simulation time period are considered the "total convection area".

2.3 Identifying open ocean polynyas across models

Since polynyas are defined as areas of open water within sea ice-covered regions, they are commonly identified based on the concentration or thickness of sea ice. A critical aspect of this identification process is determining an appropriate threshold to distinguish between open-water and ice-covered areas. A 15% sea ice concentration (SIC) threshold is often used to estimate sea ice extent (SIE) based on satellite observations and model simulations (e.g., Comiso and Nishio, 2008; Tschudi et al., 2020; Shu et al., 2020). Tamura et al. (2008) examined coastal polynyas using sea ice thickness data, defining thin ice as less

https://doi.org/10.5194/egusphere-2026-3060
Preprint. Discussion started: 10 July 2026

than 0.2 m thick and applying thresholds of 0.1 and 0.2 m to delineate their extent. Similarly, Kern et al. (2007) noted that Antarctic polynyas might include areas with ice thickness up to 0.25 m, and SIC ranging from 25% to 45%, depending on the region. Massom et al. (1998) experimented with various thresholds and concluded that a 75% ice concentration can still be effective for latent-heat polynya detection using satellite imagery. Haid and Timmermann (2013) combined SIC and ice thickness, defining polynyas as regions with less than 70% SIC or ice thickness below 0.2 m based on model outputs. Notably, Smedsrud (2005) identified polynyas with relatively high ice concentrations of 75% to 78.5%, which remained distinct within the surrounding ice-covered sea and facilitated significant ocean–atmosphere heat exchange. These varying thresholds highlight that polynya identification is inherently dataset- and method-dependent, with different data sources and detection approaches yielding substantially different results (Zhou et al., 2026).

We examine various SIC (Fig. 1c) and ice thickness (Fig. 1d) thresholds for OOP detection in the GFDL-CM4 model as a case study. Applying a relatively strict SIC thresholds between 15% and 45% limits OOP identification to the Ross sea. However, if we increase SIC threshold to 75%, we can also identify OOP in the Weddell Sea near Maud Rise. For ice thickness, using thresholds from 0.2 m to 0.5 m, we can identify OOPs in both Weddell and Ross Sea. In contrast, when a looser threshold of 0.8 m is used, OOP in the Ross Sea cannot be identified and the OOP identified in the Weddell Sea shifts from Maud Rise to southern regions. Note that most polynyas detected seem to roughly overlap with areas of deep September MLD and large MLD standard deviation.

SIC is the most widely available sea-ice-related output across models, making it a practical approach to identify polynyas. The choice of a specific SIC threshold significantly influences both polynya location and presence. To illustrate this, we test a wide range of SIC thresholds for OOP detection using the NorESM-MM model (Fig. 2). The September SIC maps (Fig. 2a) reveal regions in the Weddell and Ross Seas where SIC is substantially lower than the surrounding areas, indicating the presence of polynyas. Specifically, Specifically, one large OOP is visible in the Weddell Sea, and two smaller OOPs appear in the Ross Sea. Fig. 2c shows the OOP locations identified using different thresholds. At strict thresholds (10–30%), only the large Weddell Sea OOP is detected. Increasing the threshold to 40–50% allows detection of one OOP in the Ross Sea. If we further increase the threshold to 60–70%, the OOP in the Weddell can consistently be identified, with its size slightly increasing. However, the previous detected Ross Sea polynya disappears, and another smaller polynya closer to the Antarctic continent shows up. At very loose thresholds (80%), more locations can be classified as open water, causing the previously identified OOPs to merge with the open sea and thus no longer qualify as a polynya. The total detected polynya area initially increases with the threshold, peaks, then suddenly declines to zero when the threshold becomes too loose and all polynyas merge with open water (Fig. 2b). This kind of phenomenon has also been found by previous studies (e.g., Mohrmann et al., 2021; Landrum et al., 2026).

We perform the OOP identification test over a wide range of SIC thresholds to all 49 CMIP6 models (more details in Appendix B) and find that in general the resulting size of the detected total polynya area will rise as the threshold increases, However, overly high thresholds can cause polynyas to merge with the open ocean and become undetectable, no longer qualify as polynya. Across models, variations in SIC value distribution influence polynya detection. Models with more low-concentration

https://doi.org/10.5194/egusphere-2026-3060
Preprint. Discussion started: 10 July 2026

ice tend to show larger polynya areas at low thresholds, while those dominated by high-concentration ice only show abrupt changes when higher thresholds are applied.

Our results suggest that a universal fixed SIC threshold cannot be consistently applied across models. Here we take the long-term baseline September SIC values specific to each model into account to establish a consistent criterion applicable to all model outputs. We calculate the temporal and spatial mean SIC over all locations with sea ice cover (where SIC is larger than 0%) in each model (orange vertical line in Fig. B1). This threshold varies significantly across models, ranging from approximately 50% to around 80%. Additionally, we focus on OOPs, specifically excluding coastal polynyas connected to the Antarctic continent or ice shelf from our analysis.

3 Deep convection and OOP in CMIP6 models

We apply the methodology described in the previous section to the 49 models included in this study to identify the deep convection regions and the OOP regions in the Southern Ocean in each model. Additionally, we calculate the mean state of key SO properties, both for the SO basin (south of 55°S) and specifically within the detected deep convection and OOP regions, to analyze their relationship with convection and OOP events.

3.1 Spatial distribution of deep convection and OOP

We detect deep convection and OOP events occurring during September in models. Total convection and OOP areas are defined as the domains of all grid cells where deep convection or OOP events are detected in any year within the analyzed simulations. Figures 3 and 4 present these detections as frequency of occurrence maps, indicating how often each grid cell is classified as a convection or OOP region.

We identify deep convection in 38 out of 49 CMIP6 models (Fig. 3). Among these models, the Weddell Sea emerges as the most prominent region for the occurrence of deep convection, with 32 models indicating its occurrence. Furthermore, 18 models show deep convection in the Ross Sea, while 16 models demonstrate similar activity within the Indian Ocean sector. Models with POP-based ocean module show no convection regions.

We identify OOPs in 44 of 49 models. However, 11 models simulate just tiny polynyas, while only 33 models show OOPs clearly visible in the maps shown in Fig. 4. Consistent with previous observational studies (e.g. Carsey, 1980; Comiso and Gordon, 1996; Jena et al., 2019), OOPs occur predominantly in the Weddell Sea near Maud Rise and the Cosmonaut Sea. The Weddell Polynya appears in 26 models, with 15 simulating substantially larger polynya areas than those observed. Additionally, large polynyas in the Ross Sea region are found in 22 models. OOPs are also identified in the Indian Ocean sector of the SO in 12 models, though only 6 simulate polynyas of appreciable size, while the others show only small openings. The FGOALS-g3 model stands out for its extensive representation of polynya locations, featuring OOPs across nearly all regions of the Southern Ocean. No large OOPs are detected in the POP-based models.

The spatial resolution of models appears to influence the representation of OOP and deep convection in the SO. Among the models studied, GFDL-CM4, HadGEM3-MM, and CNRM-CM6-1-HR have the highest horizontal resolutions, with a

https://doi.org/10.5194/egusphere-2026-3060
Preprint. Discussion started: 10 July 2026

horizontal grid spacing of approximately 0.25°. All three models simulate extensive convection and some polynya formation in the Weddell Sea. The high-resolution GFDL-CM4 produces smaller convection area and smaller polynya area compared to its lower resolution counterpart, GFDL-ESM4 (0.5°), despite sharing similar physical parameterizations. Similarly, the higher-resolution HadGEM3-MM shows reduced convection and polynya extent relative to the lower-resolution HadGEM3-LL (1°). Among the CNRM models, CNRM-CM6-1-HR simulates convection and a small polynya in the Weddell Sea, while the coarser CNRM-CM6-1 (1°) simulates convection also in the Australian domain but no polynyas anywhere. By contrast, CNRM-ESM2-1 (1°) shows polynyas and significant convection in both the Australian and Weddell regions. Another example is found in the MPI-based models, where the high-resolution MPI-ESM1-2-HR (0.5°) simulates slightly smaller convection and polynya areas than MPI-ESM1-2-LR (1°), with convection and polynyas in both the Ross and Weddell Sea domains. Previous studies have reported that increased oceanic resolution can improve model performance in simulating key oceanic processes, particularly by better representing mesoscale eddy fields and dense water overflows (Dufour et al., 2017), which are crucial for the formation and maintenance of OOPs and deep convection in the SO.

Several previous studies also explored the model performance in simulating polynyas and/or deep convection in the SO from models. Some of them were using CMIP5 models, some of them were using CMIP6 models but studied different experiments (e.g. "historical").

de Lavergne et al. (2014) studied deep convection events in CMIP5 models across ‘piControl’, ‘historical’ and ‘rcp85’ experiments, using an MLD-based detection method that we also adopt. Many CMIP6 models share ocean components with their CMIP5 predecessors and exhibit similar convection locations, though CMIP6 simulations often produce slightly larger convection areas. For example, MOM-based models (e.g., ACCESS, GFDL) maintain consistent convection patterns, while others show significant changes. FGOALS-g3, MIROC6, and MPI models simulate broader convection compared to their CMIP5 counterparts, whereas CMCC and GISS models show reduced or absent convection in CMIP6. CNRM models vary with resolution with the lower-resolution CMIP6 model (CNRM-CM6-1) shifts convection to the SO Indian Ocean sector, and IPSL models display notably different convection patterns between generations.

Reintges et al. (2017) also examined deep convection in CMIP5 "piControl" runs but using different definition of MLD (depth of the ocean where the potential density difference to the surface reaches 0.01 $\mathrm{kg/m^3}$) and a stricter MLD threshold (3000 m). Their results show smaller convection areas compared to results from de Lavergne et al. (2014) and ours, though spatial patterns are broadly consistent.

Heuzé (2021) assessed SO bottom water characteristics in CMIP6 "historical" simulations, and they also laid out the locations where MLD is larger than 2000 m in their Figure 1. Notice they used a different MLD definition (depth where potential density differs from that at 10 m depth by more than 0.125 $\mathrm{kg/m^3}$). Despite differences in MLD definitions, our results largely agree in location but show larger convection areas, likely due to our longer analysis period (500 vs. 165 years). Some discrepancies remain in specific models, such as CNRM-ESM2-1, GFDL-ESM4, GFDL-CM4, and HadGEM3-GC31-LL.

Mohrmann et al. (2021) investigated SO polynyas in CMIP6 "historical" simulation. They used a strict 30% SIC threshold for polynya detection. Given our more relaxed criterion and longer simulation period, we detect larger polynya extents in

https://doi.org/10.5194/egusphere-2026-3060
Preprint. Discussion started: 10 July 2026

similar regions, especially in ACCESS, GFDL, and MPI models. Both studies find that POP-based models lack open-ocean polynyas.

3.2 Comparison of the deep convection and OOP spatial patterns

OOP events are generally attributed to heat transport from the deep ocean, where destabilization of the water column triggers deep convection. Based on this, we assume that models simulating polynyas should also exhibit deep convection. By comparing the maps of deep convection (Fig. 3) and the maps of OOP (Fig. 4), we observed a general spatial co-occurrence between polynyas and deep convective activity. Despite this overall consistency, notable inter-model differences exist in the simulation of both OOPs and convection areas.

Models employing the MOM or MPIOM ocean modules consistently simulate extensive deep convection areas alongside polynyas, typically co-located. Among these, MPIOM-based models exhibit the largest polynyas and the most significant convection activity. Within the MOM-based group, substantial polynyas are observed, although the ACCESS family of models tend to produce relatively smaller polynyas. NEMO-based models show considerable variability in both convection and polynya extent, while CanESM models simulate some deep convection but do not generate polynyas. In contrast, POP- and HYCOM-based models simulate neither convection nor polynyas.

Models from the MIROC family (MIROC6, MIROC-ES2L, and MIROC-ES2H) simulate extensive deep convection near the continental shelves of both the Ross and Weddell Seas but do not produce large polynyas. This discrepancy coincides with a markedly reduced winter sea ice extent, confined closely to the Antarctic coastline. Such behavior in MIROC models is linked to anomalously warm sea surface temperatures (Fig. 5a), and is attributed to underestimated mid-level cloud cover and excessive downward shortwave radiation (Tatebe et al., 2019), and is consistent with prior findings for MIROC5 from the CMIP5 generation (de Lavergne et al., 2014).

Similarly, the CNRM-CM6-1 model exhibits deep convection with mixed layer depths exceeding 2000 m in the Cosmonaut region but fails to produce polynyas there despite the presence of sea ice.

These examples highlight that while deep convection is a necessary condition, sometimes it is not sufficient for polynya development. Furthermore, a few models simulate polynyas without accompanying deep convection, indicating that alternative mechanisms may also contribute to polynya formation in certain cases.

3.3 Model inter-comparison of mean state

As expected, in the entire SO (here we include all locations within south of 55°S), SIC and ice thickness both decrease with increasing SST (Fig. 5a, c), with a stronger relationship for SIC-SST (Fig. 5c). Models with less sea ice or higher mean September MLD also show greater heat loss from the ocean (Fig. 5b, d). Within the total convection area, the strong negative correlation between SIC and SST, and between SIC and ocean heat flux (Fig. 6a, b) persists. While both SIC and ice thickness correlate with ocean heat flux, SIC is the stronger predictor in both cases.

To investigate what controls the extent of the convection area across models, we use three separate convective area metrics. The first is maximum convection area, defined as the largest area of a convection event across all years, and reflects the

https://doi.org/10.5194/egusphere-2026-3060
Preprint. Discussion started: 10 July 2026

maximum potential size of a convective event in a model. The second is mean convection area, defined as the average convection event size across all years (including years with no events), which indirectly incorporates the temporal frequency of convection. The third is the total convection area. In general, we find reasonable correlations between the maximum, mean and total convective area across models. Models with larger maximum convection areas tend to exhibit larger mean areas. However, some models may produce only one large event during the entire simulation and no small events, resulting in a large maximum area but small mean convection area.

Models with larger mean convective areas tend to have higher SST (both September and annual mean), deeper September MLD and greater September heat loss within convective regions (Fig. 6d-f). These results broadly align with the established understanding of Southern Ocean convection: enhanced vertical mixing brings warm Circumpolar Deep Water (CDW) to the surface, increasing SST, melting sea ice, and enhancing heat loss to the atmosphere. However, the relationships are not uniform. For example, CAS-ESM2-0 (No.15), FGOALS-g3 (No.16), HadGEM3-GC31-MM (No.22), and CNRM-CM6-1 (No.30) exhibit relatively small mean convection areas but high heat flux loss, suggesting that additional mechanisms are involved.

Models with larger mean convective areas also show lower September SIC south of 55°S (Fig. 6c). One possible explanation is that reduced SIC allows subsurface heat to melt sea ice more effectively, exposing the ocean surface to wind-driven mixing and cooling, which promotes convection. Alternatively, larger convective areas may enhance upward heat transport, accelerate sea ice melt and further reduce SIC.

4 Coupling between deep convection and OOP events across CMIP6 models

We observe that in many models, the spatial distribution of deep convection and OOP events overlap significantly. Furthermore, a comparison of the total OOP and deep convection areas across models reveals a positive relationship: models with larger total polynya areas generally also show more deep convection regions (Fig. 7a). This positive corelation supports the interpretation that OOPs are sensible heat polynyas formed by upwelling of warmer deep waters, consistent with previous studies (e.g. Morales Maqueda et al., 2004). However, we also notice that in most cases, the total convective areas are larger than the total OOP areas, as indicated by most models falling below the 1:1 line in Fig. 7a. This discrepancy suggests that the relationship between deep convection and OOP may be more complex than a simple one-to-one correspondence.

To further examine whether OOPs are sensible heat flux driven by upwelling of warm deep waters, we analyze the spatial and temporal co-occurrence of deep convection and OOP events. For each model and simulation year, we detect the presence of both event types and calculate the cumulative area of all convection and all OOP events over the analyzed simulation period. We also identify regions where deep convection and OOPs co-occur in the same year, representing spatial-temporal overlap, and compute the cumulative area of these overlapping events. To quantify the degree of overlap, we calculate the ratio of this overlap area relative to the cumulative area of all OOP events and to the cumulative area of all deep convection events.

For most models, the ratio of overlap area relative to the cumulative area of all deep convection events is low (Fig. 7b), indicating that the majority of deep convection events are not associated with OOP formation. Several factors may explain the limited association between deep convection and OOPs, varying across models.

https://doi.org/10.5194/egusphere-2026-3060
Preprint. Discussion started: 10 July 2026

First, deep convection may not release enough heat to melt sufficient sea ice to form a detectable polynya. This can be observed in the GFDL-CM4 model, where strong and repeated convection events occur in the Weddell Sea. However, although the overlaying SIC decreases during the convection events, the dropping of SIC is insufficient to meet the required threshold for polynya detection.

Second, although ice melt occurs above convection area, the resulting open-water region may be too large and merge with the surrounding open ocean, making it indistinguishable as a discrete polynya under our detection algorithm. For example, in the GFDL-CM4 model, polynyas are detected in the Ross Sea during model year 235. However, in model year 236, despite the presence of deep convection in the same region, the overlying sea ice has melted substantially, creating an open-water area the connects to the broader SO. As a result, no polynyas are detected in that year.

Third, some OOP events may form independently of deep convection, instead driven by wind-induced sea ice divergence. These cases are likely confined to the surface mixed layer, without involving deeper ocean overturning. To investigate this further, we analyze the ratio of the overlap area relative to the cumulative area of all OOP events.

The ratio of overlap area relative to the area of all OOP events varies strongly across models. We define the overlapping regions, where OOP events coincide with deep convection, as **deep OOPs**, since the underlying MLD is necessarily deep. However, in many cases, OOP events occur without concurrent deep convection and instead have very shallow MLDs, suggesting that these are not classical, thermally driven "sensible heat polynyas". By extension, OOPs without deep convection are termed **shallow OOPs**, and are associated with relatively shallow MLDs. Thus, the ratio of overlap area to the aera of all OOP evnets provides a measure of the fraction of deep OOPs among all OOPs.

Classifying polynyas into deep and shallow categories offers a more straightforward and process-based distinction, as it better separates the dominant dynamics of polynya formation than the traditional latent heat (usually associated with OOP) vs. sensible heat (usually corresponding to coastal polynyas) classification (Morales Maqueda et al., 2004). In reality, both coastal and open-ocean polynyas involve a combination of sensible and latent heat processes.

Within CMIP6, some models exhibit almost no deep OOPs, while others, such as four MOM-based models (No. 2–5) and two MICOM-based models (No. 42 and 43), show extensive deep OOP coverage (Fig. 7b). In these models, more than 70% of the OOPs are deep, with shallow OOPs comprising less than 30%.

We further analyze major oceanic properties, focusing on the differences between deep and shallow OOPs within each model, and across models (Figure 8). In all models, deep OOPs consistently show deeper September MLD and higher September SSS, which is consistent with warmer water upwelling. SST is also generally higher in deep OOPs, except for MIROC6 (No. 47), which are very warm models with anomalously high SST across the entire SO. Similarly, oceanic heat flux loss tends to be greater in deep OOPs across models, with exceptions being UKESM1-1-LL (No. 24) and MIROC6 (No. 47). As expected, SIC is lower in deep OOPs in all models, except for MIROC6 (No. 47).

These findings collectively support our central hypotheses that: (a) saltier surface waters can destabilize the water column and trigger deep convection, resulting in OOPs; and (b) in deep OOPs, a deeper MLD and enhanced vertical mixing engage more of the warm, saline upper CDW layer than in shallow OOPs, which results in warmer and saltier surface waters and a more significant reduction in sea ice cover compared to shallow OOPs.

https://doi.org/10.5194/egusphere-2026-3060
Preprint. Discussion started: 10 July 2026

5 Summary of model properties by ocean module group

Differences in models coupling methods, the use of various ocean and sea ice modules, and parameterization used to simulate key mixing processes can all contribute to the discrepancies of the performance in different models. Parameterization, which involves approximating physical processes within model equations, varies significantly across different ocean module in the models. Their assumptions differ regarding the mechanisms of surface and deep water mixing, as well as buoyancy-driven convection. Here, we will discuss some model groups based on the ocean module used and address some particularly noteworthy behavior in different groups.

5.1 MOM-based models

The Modular Ocean Model (MOM), developed by NOAA's Geophysical Fluid Dynamics Laboratory (GFDL), is an ocean circulation model that employs a structured latitude-longitude grid and finite-volume difference methods with explicit time stepping to solve the primitive equations of motion. MOM incorporates several parameterizations, including the Gent-McWilliams (GM) mesoscale eddy parameterization and the K-profile parameterization (KPP) for vertical mixing (Adcroft et al., 2019).

The latest version MOM6 used in the two GFDL models. Unlike earlier versions that utilized a B-grid, MOM6 adopts a horizontal C-grid, which is preferred for simulations that include an active mesoscale eddy field. Additionally, MOM6 employs a vertical Arbitrary Lagrangian-Eulerian (ALE) remapping technique, allowing for the use of any vertical coordinate system, including geopotential, isopycnic, terrain-following, or hybrid/user-defined grids. This flexibility enhances the model's ability to accurately represent ocean dynamics, particularly in regions with complex bathymetry or varying stratification, which is crucial for accurately modeling processes such as ice shelf grounding lines and coastal estuaries (Griffies et al., 2020).

The MOM-based models (No.1 BCC-CSM2-MR, No.2 BCC-ESM1, No.3 CAMS-CSM1-0, No.4 ACCESS-ESM1-5, No.5 ACCESS-CM2, No.6 GFDL-CM4, No.7 GFDL-ESM4) show relatively large mean convective areas. Within MOM-based models, models with deeper September MLD also tend to simulate larger convective regions (Fig. 6e). While these models have averaged mean SIC among all CMIP6 analyzed models, this group has the lowest mean sea ice thickness within south of 55°S across all models (Fig. 5c). This reduced ice thickness likely facilitates deep convection by lowering the energy barrier required for ice melt, which may account for the substantial total convection and polynya areas observed in MOM-based models.

Within MOM-based models, BCC-ESM1, CAMS-CSM1-0, ACCESS-ESM1-5, and ACCESS-CM2 demonstrate that over 70% of OOPs are classified as deep OOPs, consistent with the presence of high MLDs. Conversely, the two GFDL models (GFDL-CM4 and GFDL-ESM4) feature moderate MLDs south of 55°S (less than 250 m) and correspondingly smaller convective areas, suggesting a distinct convective regime relative to the other MOM-based models.

https://doi.org/10.5194/egusphere-2026-3060
Preprint. Discussion started: 10 July 2026

5.2 LICOM-based models

The LASG/IAP Climate System Ocean Model (LICOM) employs a structured grid with finite difference discretization and explicit time stepping, including the isopycanal mixing and GM scheme for mesoscale eddy parameterization and Canuto scheme for vertical mixing (Liu et al., 2012; Lin et al., 2020).

Two LICOM-based models are used in this study: the CAS-ESM2-0 (No. 15) and FGOALS-g3 (No. 16). FGOALS-g3 is using the latest LICOM3 module, and it stands out as the coldest and saltiest model within south of 55°S (Fig. 5a), showing also the highest surface salinity in this region, including within convective and polynya area. These characteristics contribute to its high convective activity, as indicated by substantial surface heat loss both south of 55°S (Fig. 5b) and within convective regions (Fig. 6f). Despite strong convection, SIC remains high (70% or above) both south of 55°S and within the convective area, due to the model's persistently low SST.

In contrast to most models, FGOALS-g3, along with two MPIOM-based models, is distinguished by a total OOP area exceeding the total convective area, with FGOALS-g3 having the largest total OOP area among all models (Fig. 7a). This feature leads to the highest overlap between convection and OOP with over 50% of the convective area corresponds to OOPs (Fig. 7b). However, only 18% of OOPs detected in the model are classified as deep OOPs, indicating that while polynyas are widespread, deep convection is more localized within them. Overall, the FGOALS-g3 model is characterized by a relatively low average SIC, an extensive polynya coverage, and a substantial convective region, highlighting its distinct ocean-ice interaction dynamics relative to other models.

5.3 NEMO-based models

The Nucleus for European Modelling of the Ocean (NEMO) is developed as a collaborative effort among European institutions. In our study, a total of 20 models incorporate ocean modules based on NEMO. These NEMO-based models use a geopotential vertical gird and implement a turbulent kinetic energy (TKE) scheme for vertical mixing (Uotila et al., 2017). Although 12 of these models (model No. 25-36) employ the same NEMO version 3.6, there are substantial variability in their simulations of deep convection and OOP events. Previous studies have found that modifying the oceanic vertical mixing parameters in NEMO model can greatly influence the extent of SO open-ocean deep convection and the process triggering it (Heuzé et al., 2015).

Among this large group of models, two models from Met Office Hadley Centre (MOHC), HadGEM3-GC31-LL (No. 21) and HadGEM3-GC31-MM (No.22), stand out. These two models have similar model settings, differing primarily in horizontal resolution: HadGEM3-GC31-MM operates at a higher resolution (grid spacing of approximately 0.25°) compared to HadGEM3-GC31-LL (1°). While HadGEM3-GC31-LL exhibits deep convection across all major basins, HadGEM3-GC31-MM has a smaller total deep convection area, localized to the Weddell Sea in the Atlantic sector (Fig. 3).

Within the SO basin (south of 55°S), the higher-resolution HadGEM3-GC31-MM (No. 22) shows warmer and saltier surface waters, reduced SIC(50% vs. 56%), and increased surface heat loss (45 vs. 38 $\mathrm{W/m^2}$) relative to HadGEM3-GC31-LL (No. 21). These contrasts are even more pronounced within convective regions, where HadGEM3-GC31-MM also shows signifi-

https://doi.org/10.5194/egusphere-2026-3060
Preprint. Discussion started: 10 July 2026

cantly deeper MLD (1000 m vs. 200 m), slightly larger mean convective areas, elevated SST, thinner ice cover, lower SIC (20% vs. 70%), and approximately threefold greater surface heat flux loss (100 vs. 35 $\mathrm{W/m^2}$) compared to HadGEM3-GC31-LL.

Interestingly, despite extremely high MLDs ($>$ 2300 m) inside polynyas in model 22, the proportion of deep OOPs is low. This suggests a disconnect between MLD and deep polynya formation, warranting further investigation.

5.4 BLOM-based Models

The Bergen Layered Ocean Model (BLOM) employs a C-grid spatial discretization with 51 isopycnal layers and uses the KPP scheme for vertical mixing, with increased maximum allowable mixing near the ocean bottom to provide sufficient mixing downstream of overflows (Seland et al., 2020).

Three BLOM-based models from the Norwegian Climate Centre (NCC) are included in this study: NorCPM1 (Model No. 41), NorESM2-MM (No. 42), and NorESM2-LM (No. 43). NorCPM1 is a coupled climate prediction model that incorporates data assimilation. NorESM2-MM and NorESM2-LM are fully coupled Earth system models, with NorESM2-MM featuring higher spatial resolution for the atmosphere and land components. Both models share identical resolution for ocean and sea ice components.

While no deep convection is detected in NorCPM1, NorESM2-MM and NorESM2-LM show strong deep convection and rank among the most convective models. They show high MLD (deeper than 1700 m) in both convective and polynya regions, along with relatively large mean convective areas. While their SST, SIC, and heat flux loss in convective regions are close to the multi-model mean, they show strong spatial and temporal alignment between polynya occurrence and deep convection. In both models, 70-80% of OOPs are deep OOPs, and around 30% of the total convective area is associate with OOP formation, among the highest across all models. These models also show high polynya frequency (70-90% of the time), with frequent temporal co-occurrence of large OOP and large convective events.

5.5 MPIOM-based Models

The three MPIOM-based models from the HAMMOZ-Consortium and the Max Planck Institute for Meteorology provide a useful inter-model comparison due to their consistent configurations but differing horizontal resolutions. Among the three models, MPI-ESM1-2-HR (No. 45) has the highest spatial resolution at approximately 0.5°, while MPI-ESM1-2-LR (No. 46) and MPI-ESM1-2-HAM (Model 44) both have coarser resolutions near 1°. All three models use a modified version of the Pacanowski and Philander (PP) ocean vertical mixing scheme (Gutjahr et al., 2021). MPI-ESM1-2-HAM distinguishes itself through its more sophisticated aerosol scheme, which may lead to differences in climate sensitivity compared to the other two models.

MPI-ESM1-2-HAM shows the warmest SO September SST, the lowest SIC, deepest MLD, and most heat flux loss among the three models, but instead has the smallest mean polynya area. This likely results from its reduced SIE, which limits the formation of OOPs within the Weddell Sea. The model's relatively warm SST promotes extensive ice melt, merging open water with the large open ocean and thereby not being identified as OOPs by our identifying algorithm.

https://doi.org/10.5194/egusphere-2026-3060
Preprint. Discussion started: 10 July 2026

MPI-ESM1-2-HR and MPI-ESM1-2-LR show large total OOP areas that exceed their respective total convective areas. However, these models display relatively shallow MLDs and limited spatial overlap between OOP and convection events, with less than 10% of OOPs classified as deep OOP.

5.6 COCO-based Models

The three Japanese climate models, MIROC6 (No. 47), MIROC-ES2L (No. 48), and MIROC-ES2H(No. 49) are based on the CCSR Ocean Component Model (COCO), an ocean general circulation model using the geopotential height vertical coordinate and incorporate a turbulence closure scheme (Tatebe et al., 2019).

Compared to other models, these three show the warmest sea surface temperatures (SST) and the lowest SIC south of 55°S, with SIC typically below 15% and relatively thin ice layers ranging from 0.6 to 0.8 meters. These characteristics are consistent with previous studies (Beadling et al., 2020; Mohrmann et al., 2021). MIROC6 (No. 47) shows the highest surface heat flux loss among all models, likely due to its combination of low sea ice cover and deep mixed layer depth (MLD).

Within convective regions, these models also maintain relatively high SST, low SIC, and elevated MLD values. MIROC6 and MIROC-ES2H have some of the largest mean convective areas, with MIROC6 also showing the highest heat flux loss within convective regions. The combination of excessive surface warmth and reduced ice cover in these models results in the near absence of well-defined polynyas. Instead, the SO behaves more like a persistent polynya. Deep convection occurs widely across the SO during winter and persists throughout the season.

Interestingly, MIROC-ES2L (No. 48) differs somewhat from its counterparts. Although it features high MLD and a relatively large convective area, it shows lower SST and SSS. These fresher surface conditions likely contribute to its comparatively weaker and less extensive convection. MIROC-ES2L simulates the smallest total convective area among the MIROC models, highlighting the critical role of SSS in modulating convection dynamics.

5.7 MPAS-Ocean models

The Model for Prediction Across Scales-Ocean (MPAS-Ocean) is the ocean component of the Energy Exascale Earth System Model (E3SM) that developed by the U.S. Department of Energy. MPAS-Ocean uses an unstructured Voronoi mesh with an Arakawa C-grid discretization, allowing variable horizontal resolution and enabling high-resolution regional refinement. It employs a z-star vertical coordinate, and incorporates the K-profile parameterization (KPP) for vertical mixing (Ringler et al., 2013; Golaz et al., 2022). Three models emplyed MPAS-Ocean are included in this study: E3SM-1-0, E3SM-2-0, and E3SM-2-0-NARRM. The two E3SM-2-0 models use a more recent MPAS-Ocean version, with the NARRM variant featuring the North American regionally refined mesh grids. All three models in our study operate at similar low spatial resolutions, with mesh spacing ranging from 30 to 60 km.

Previous studies with the low-resolution E3SM v1 model has demonstrated that low-resolution configurations poorly represent Antarctic coastal polynyas (Jeong et al., 2020). However, a high-resolution E3SM v1 (E3SM-HR, mesh spacing 8-16 km) show significant improvements in simulating coastal polynyas relative to their low-resolution counterparts (Jeong et al., 2023). As for OOPs, the low-resolution E3SM-LR simulations fail to reproduce OOP events, whereas E3SM-HR successfully simu-

https://doi.org/10.5194/egusphere-2026-3060
Preprint. Discussion started: 10 July 2026

lates OOP occurrences near Maud Rise (Jeong et al., 2023). Consistent with these findings, none of the three low-resolution models in our study produce OOPs. Although minor ice openings appear in E3SM-1-0, these are likely artifacts resulting from our use of a relatively loose sea ice concentration threshold (50% versus 15% in previous studies) and represent negligible, small-scale events. Furthermore, none of the models show deep convection. All three models as a group also show some of the lowest heat flux loss, MLD and SSS of all the models.

5.8 POP-based Models

The Parallel Ocean Program (POP) is a numerical ocean model developed primarily at Los Alamos National Laboratory (LANL) and optimized for efficient simulation on massively parallel computing architectures. POP employs fixed-depth (z-level) vertical coordinates and use KPP scheme for vertical mixing (Danabasoglu et al., 2020).

In this study, we examine six POP-based models, four of which are versions of the Community Earth System Model 2 (CESM2) featuring different atmospheric configurations. CESM2 incorporates an overflow parameterization scheme that facilitates the transport of dense bottom water down continental shelves, enhancing the realism of bottom water formation processes(Danabasoglu et al., 2020). While Mohrmann et al. (2021) demonstrated that CESM2 can reproduce coastal polynyas, we find that POP-based models, including various CESM2 versions, can not simulate either OOPs or deep convection events, consistent with studies on multiple generations of POP-based models in CMIP5 and CMIP6 (e.g., de Lavergne et al., 2014; Heuzé, 2021; Mohrmann et al., 2021).

Interestingly, Chang et al. (2020) found that a high-resolution configuration of CESM (CESM1.3, with 0.1° horizontal resolution) can simulate intermittent occurrences of sizable OOPs in the Weddell Gyre. This suggests that the Weddell Polynya may play a important role in regional and global climate dynamics, as proposed by Latif et al. (2013), and that some models may underrepresent this phenomenon. Future CESM generations will be based on the MOM6 ocean model with isopycnal coordinates, which has demonstrated improvements in deep water properties and is expected to enhance Southern Ocean water mass representation.

6 Conclusions

Despite the significant climatic influence, OOP remains poorly represented in many climate models, and their relationship with deep convection remains uncertain. In this study, we investigate the occurrence of OOPs and their connection to deep ocean convection events across 49 CMIP6 models under long term "piControl" simulations. To ensure consistent detection, we evaluate multiple identification methods and find that methodological choices substantially affect the diagnosed frequency and extent of both kinds of events. For deep convection, we assess the use of an MLD threshold. While a relatively loose criterion increases the detected convective area, it may not adequately capture the multi-decadal variability of deep convection in many models (Fig. 1). For OOP, we test using different thresholds for SIC and find that a uniform SIC threshold across all models unsuitable. Instead, we adopt a relative threshold based on the mean climatological SIC specific to each model, enabling a more consistent and meaningful detection of OOPs across diverse models.

https://doi.org/10.5194/egusphere-2026-3060
Preprint. Discussion started: 10 July 2026

Using these tailored criteria, our analysis identifies 38 models that can simulate deep convection and 40 models that can simulate OOP, although some detected OOP are tiny and may be artifacts of our detection algorithm. We find 37 models can simulate both kinds of events during the simulated period, while there are also models that simulate only deep convection or only OOPs, as we illustrated in 3.2.

Across the CMIP6 ensemble, model structure plays a decisive role. MOM- and BLOM-based models generally simulate frequent deep OOPs, whereas POP- and HYCOM-based models show neither deep convection nor OOPs. These differences likely stem from variations in vertical mixing schemes, overflow parameterizations, and ocean–ice coupling. Previous studies using NEMO-based models have shown that the choice of sea ice module can influence ocean circulation, particularly in regions where sea ice strongly affects water mass formation and deep convection (Uotila et al., 2017). In our results, while the occurrence of OOP varies with the sea ice module used, this effect is not consistent across models and the occurrence or absence of OOP does not appear to be systematically determined by the ice module type alone. This suggests that differences in OOP representation arise not only from the ice model architecture but also from model-specific coupling mechanisms between ocean and sea ice and surface flux parameterizations.

Our analysis of the SO mean state across CMIP6 models reveals expected relationships among SST, SIC, ice thickness, and MLD. Specifically, increased SST is associated with reductions in both SIC and sea ice thickness, while regions with deeper MLD tend to have greater oceanic heat loss and reduced September sea ice. These relationships are robust both across the broader SO (south of 55°S) and specifically in areas experiencing deep convection, indicating strong and consistent coupling between thermal and ice processes. This suggests that surface thermal and ice-related conditions play a key role in modulating the spatial extent of deep convection events. We also examine the size of deep convective regions in relation to SIC, SST, MLD, and downward heat flux, and find consistent associations. In general, deep convection events are linked to lower SIC, higher SST, deeper MLD, and increased oceanic heat loss.

When examining the size of deep convective regions, we find no significant correlation with mean SSS and mean ice thickness across the SO. However, we assess the relationship between SSS and ice thickness and find positive correlation between these two factors inside the convection regions, and in general within convective region, the SSS is basically higher, and ice thickness is basically lower, which suggesting deep convection events tend to occur in regions of elevated SSS and strong surface cooling.

The causal direction of these relationships remains unclear. For example, it is not yet known whether elevated SSS and heat loss precondition the ocean for convection, or whether the convective process itself leads to surface salinification and heat release. Resolving this ambiguity will require detailed temporal diagnostics, including lagged correlations and causality analyses. In future work, we aim to apply such diagnostics to individual CMIP6 models in order to disentangle the relative contributions of thermal and salinity-driven preconditioning mechanisms in initiating deep ocean convection and linking it to OOP formation.

Although OOPs are often viewed as the result of deep convection, and are commonly classified in the literature as sensible heat polynyas, driven primarily by thermal processes (Morales Maqueda et al., 2004), our analysis shows that only a subset of deep convection events coincide with OOP formation. Conversely, many OOPs occur without concurrent deep mixing. In

https://doi.org/10.5194/egusphere-2026-3060
Preprint. Discussion started: 10 July 2026

reality, both coastal and open-sea polynyas involve a combination of sensible and latent heat fluxes, making the classification into sensible or latent heat types somewhat ambiguous. To distinguish between these cases, we introduce the terms deep OOP and shallow OOP, depending on whether an OOP coincides with a deep convection event in the same year. As expected, deep OOPs exhibit significantly deeper September MLDs and higher SSS compared to shallow OOPs, consistent with enhanced vertical mixing and surface salinification. This classification provides a useful diagnostic for linking surface polynya behavior to subsurface convective dynamics.

In the observational record, dense water formation in the SO primarily occurs via shelf processes, particularly in the Weddell, Ross, and Adélie regions, where high salinity shelf water sinks to form AABW. However, models in CMIP5 and CMIP6 typically produce deep and bottom waters through open-ocean deep convection that is too strong, too frequent, or too spatially extensive compared to observations (Heuzé, 2021). This "unrealistic" convection often coincides with excessively large or frequent OOPs, particularly in the Weddell or Ross Sea. Following the CMIP5 inter-comparison, many modeling groups implemented parameterizations to suppress excessive open-ocean convection (e.g., Held et al., 2019, in GFDL-CM4,). However, our analysis indicates that some CMIP6 models still exhibit substantial open-ocean convection. Mohrmann et al. (2021) reported similar findings, showing that most CMIP6 models overestimate the size and persistence of the Weddell Polynya—except for models such as GFDL-CM4 and IPSL-CM6A-LR, which simulate sub-ice convection, and MIROC models, which tend to remain ice-free.

Despite these biases, our results suggest that deep OOPs, through their extreme MLDs and strong overturning, may contribute to bottom water formation in models, thereby affecting global overturning circulation and, consequently, the global climate system. This has also been demonstrated in recent studies, where high-resolution models showed an increased occurrence of OOPs in the SO (Chang et al., 2020; Diao et al., 2022; Jeong et al., 2023). In those simulations, deep polynyas were shown to serve as direct sites of AABW formation, suggesting that the connection between OOPs and deep water production is physically plausible under certain conditions. Our study aligns with these findings and supports the hypothesis that SO OOPs play an active role in both regional and global climate (Latif et al., 2013; Chang et al., 2020).

Previous analyses on CMIP5 and CMIP6 models have shown that anthropogenic forcing tends to suppress deep convection in the SO due to surface freshening, leading to a transition from active open-ocean convection in pre-industrial climates to a more stratified ocean state under future warming scenarios (de Lavergne et al., 2014; Chen et al., 2023). We anticipate a similar decline in both deep and shallow OOP activity under increasing greenhouse gas forcing. Such a shutdown could lead to multi-decadal accumulation of heat, salt, nutrients, and carbon in the deep Southern Ocean, with important implications for global heat and carbon budgets (e.g., Bernardello et al., 2014). Continued evaluation of OOPs and deep convection across CMIP6 and higher-resolution models will therefore be critical for understanding the future evolution of Southern Ocean overturning and its role in climate regulation.

While many models show strong coupling between OOPs and deep convection events, others clearly fall into regimes characterized by shallow or absent convection, highlighting substantial inter-model diversity. The variability in coupling strength demonstrates that OOP occurrence alone is not a sufficient indicator of deep ocean mixing. Instead, both large-scale mean-state properties such as stratification, surface buoyancy fluxes, and sea ice conditions, and model structural choices jointly determine

https://doi.org/10.5194/egusphere-2026-3060
Preprint. Discussion started: 10 July 2026

whether and how these phenomena co-occur. Therefore, understanding SO variability requires not only tracking individual processes, but also diagnosing their coupled behavior within each model framework. Looking forward, extending this analysis to transient climate simulations will be critical for assessing how the interplay between OOPs and deep convection evolves under anthropogenic forcing, and for improving confidence in projections of Southern Ocean overturning and its role in the global climate system.

Code and data availability. The code used for the analysis in this study is openly available on GitHub. The CMIP6 data used in this study were obtained from the Earth System Grid Federation (ESGF) archives, Google Cloud Storage, and NCAR CISL's GLADE disk storage. The datasets available on Google Cloud are maintained by the Climate Data Science Lab at the Lamont-Doherty Earth Observatory (LDEO) of Columbia University and are derived from the original CMIP6 datasets hosted by ESGF.

Appendix A: Calculation of MLD based on model diagnostic variables

The diagnostic variable "mlotst" representing the "ocean mixed layer thickness defined by sigma t" is a parameter saved in many CMIP6 models. However, the methodology used to derive this variable can vary significantly between models. Additionally, in some models, this variable is not yet available. As a result, one has to compute the MLD independently. Fortunately, almost all models offer access to monthly diagnostic variables "sea water potential temperature" ("thetao") and "sea water salinity" ("so") which enable the calculation of the monthly mean potential density, and determine the MLD systematically.

The state-of-the-art Equation of State used in marine science improves over time. The previous widely used UNESCO-80 equation of state (EOS-80) seawater toolbox developed by the Commonwealth Scientific and Industrial Research Organisation (CSIRO) used practical salinity and potential temperature as input for the equation of state to calculate potential density. EOS-80 is now considered obsolete and EOS-80 based toolbox has been replaced by the Gibbs SeaWater (GSW) Oceanographic Toolbox based on the International Thermodynamic Equation Of Seawater 2010 (TEOS-10), which requires conservative temperature and absolute salinity as input for the equation of state.

However, a number of CMIP6 models retain the use of the EOS-80 method (Griffies et al., 2016) and list the oceanic diagnostic salinity ("so") and temperature ("thetao") variables as practical salinity and potential temperature. Therefore, it is necessary to convert these variables into absolute salinity and conservative temperature prior to their use as input for the TEOS-10 functions. This conversion can be achieved through functions available in the TEOS-10 toolbox (e.g. "gsw_CT_from_pt", "gsw_SA_from_SP").

We apply such conversions to the original outputs from the GFDL-CM4 model, using September temperature and salinity data from the SO Weddell Sea. Such conversion can introduce notable changes(Fig. A1). After conversion, both salinity and temperature increased, but salinity showed a more pronounced increase in the deep ocean, whereas temperature increased mainly near the surface. Together, these changes leads to higher density in the deep ocean and a steeper vertical density gradient. Therefore, it results in more stabilized water column and shallower MLD compared to calculations performed based

https://doi.org/10.5194/egusphere-2026-3060
Preprint. Discussion started: 10 July 2026

on the original model outputs. In certain models, these adjustments can significantly reduce or even eliminate regions of deep convection, which is defined based on MLD.

McDougall et al. (2021) recommended interpreting the diagnostic temperature outputs from all CMIP6 models, regardless of whether they are based on EOS-80 or TEOS-10, as Conservative Temperature, and the salinity outputs as Preformed Salinity. They recommended that these outputs be used directly as inputs into the GSW toolbox for density calculations in general applications. Following this guidance, we compute the monthly potential density using diagnostic outputs from the models directly using the GSW toolbox. We then applied the criteria established by de Boyer Montégut et al. (2004) to determine the monthly MLD for each model.

Appendix B: Influence of SIC thresholds on Polynya detection

We propose that SIC thresholds for polynya detection must take into account the baseline SIC in each model. We investigate the statistical distribution of SIC in the SO for each model and test a wide range of SIC threshold to evaluate their impact on polynya identification. Figure B1 shows the histogram of non-zero September SIC values south of 40°S for all models used in this study. We find that most models show a pronounced unimodal distribution, characterized by high SIC values (e.g., above 80% or 90%) dominating ice-covered regions and very low SIC values (e.g., below 5%) marking the sea ice edge. However, a subset of models, such as MPI-ESM-1-2-HAM and MPI-ESM1-2-LR, show a relatively flat SIC distribution, with substantial areas covered by low-concentration ice. We also compute two averages for each model: (1) the mean SIC across the entire SO domain (including zero values), and (2) the mean SIC within the SIC (excluding zero values). These means vary considerably across models, highlighting differences in sea ice representation. We note that models can also be separated into broad categories according to their ice module, as indicated by the legend colors in Fig. 4.

To evaluate the sensitivity of polynya detecting threshold, we test SIC thresholds ranging from 1% to 99%. For example, a threshold of 10% classifies any grid cell with SIC below 10% as open water, and any cell with SIC above 10% as ice-covered. Similarly, a threshold of 80% includes all cells with SIC below 80% as potential polynya areas. Thus, a 10% threshold serves as a strict criterion, detecting smaller polynyas, while 80% represents a looser threshold, identifying in principle broader polynya regions.

For most models, increasing the SIC threshold results indeed in a larger number of grid cells being identified as part of a polynya. However, if the threshold becomes excessively high, regions previously identified as polynyas may merge with the open ocean, leading to their exclusion from polynya classification, as demonstrated in Fig. 2. We calculate the total OOP area in each model as the area of all grid cells that can be categorized as OOP under a given threshold during the entire analyzed simulation period. The results are shown as the blue line in Fig. B1.

We propose that the sensitivity of total OOP area to SIC thresholds is influenced by the underlying model SIC distribution. Models with extensive regions of low-concentration sea ice tend to produce larger total OOP areas at lower thresholds, with the area decreasing as the threshold increases. In contrast, models dominated by high-concentration ice show relatively small OOP

https://doi.org/10.5194/egusphere-2026-3060
Preprint. Discussion started: 10 July 2026

areas at low thresholds, followed by a sharp increase around 70-80%, peaking near 90%, and then rapidly declining. Therefore, selecting an appropriate SIC threshold for polynya detection should consider the model's baseline SIC distribution.

Appendix C: Additional correlations between ocean and sea ice properties

We present supplementary analyses examining correlations among key oceanographic and sea ice variables. The accompanying figures illustrate relationships that provide insights into model performance regarding deep convection and OOP simulations.

Specifically, the figures include scatter plots illustrating associations between variables such as SST, SSS, SIC, ice thickness, MLD, and ocean heat flux with detected OOP or deep convection regions (Figures C1, C2, C3, C4). Additionally, we analyze how the percentage of deep OOPs among all detected OOPs relates to differences in specific variables between deep and shallow OOPs (Figure C5).

Author contributions. SL, IM and SM designed the study. SL performed most of the numerical analysis and wrote the paper with support from IM and SM.

Competing interests. The authors declare they have no conflict of interest.

Acknowledgements. This work was supported by an NSF PO grant and by grants from the University of Pennsylvania. The authors would like to acknowledge support from the Penn Global Research and Engagement Grant and a Penn Environmental Innovations Initiative Research Community Grant. The authors thank the open source Pangeo project, supported by the NSF Award 1740648 for enabling direct analysis of the output of the CMIP6 model through 2024. The authors also thank NCAR CISL for allowing academic access to CMIP6 data for analysis. The authors also acknowledge the World Climate Research Program, which, through its Working Group on Coupled Modeling, coordinated and promoted CMIP6. The authors thank all climate modeling groups for producing and making available their model outputs, the Climate Data Science Lab and NCAR CISL for maintaining data storage on Google Cloud and NCAR HPC, the Earth System Grid Federation (ESGF) for archiving the data and providing access, and the multiple funding agencies who supported CMIP6 work.

https://doi.org/10.5194/egusphere-2026-3060
Preprint. Discussion started: 10 July 2026

References

Adcroft, A., Anderson, W., Balaji, V., Blanton, C., Bushuk, M., Dufour, C. O., Dunne, J. P., Griffies, S. M., Hallberg, R., Harrison, M. J., Held, I. M., Jansen, M. F., John, J. G., Krasting, J. P., Langenhorst, A. R., Legg, S., Liang, Z., McHugh, C., Radhakrishnan, A., Reichl, B. G., Rosati, T., Samuels, B. L., Shao, A., Stouffer, R., Winton, M., Wittenberg, A. T., Xiang, B., Zadeh, N., and Zhang, R.: The GFDL Global Ocean and Sea Ice Model OM4.0: Model Description and Simulation Features, J. Adv. Model Earth Syst., 11, 3167–3211, https://doi.org/10.1029/2019MS001726, 2019.

Asay-Davis, X. S., Jourdain, N. C., and Nakayama, Y.: Developments in Simulating and Parameterizing Interactions Between the Southern Ocean and the Antarctic Ice Sheet, Curr. Clim. Change Rep., 3, 316–329, https://doi.org/10.1007/s40641-017-0071-0, 2017.

Barber, D. G. and Massom, R. A.: The Role of Sea Ice in Arctic and Antarctic Polynyas, in: Polynyas: Windows to the World, edited by Smith, W. O. and Barber, D. G., vol. 74 of *Elsevier Oceanography Series*, pp. 1–54, Elsevier, https://doi.org/10.1016/S0422-9894(06)74001-6, 2007.

Beadling, R. L., Russell, J. L., Stouffer, R. J., Mazloff, M., Talley, L. D., Goodman, P. J., Sallée, J. B., Hewitt, H. T., Hyder, P., and Pandde, A.: Representation of Southern Ocean Properties across Coupled Model Intercomparison Project Generations: CMIP3 to CMIP6, J. Clim., 33, 6555–6581, https://doi.org/10.1175/JCLI-D-19-0970.1, 2020.

Behrens, E., Rickard, G., Morgenstern, O., Martin, T., Osprey, A., and Joshi, M.: Southern Ocean deep convection in global climate models: A driver for variability of subpolar gyres and Drake Passage transport on decadal timescales, J. Geophys. Res. Oceans, 121, 3905–3925, https://doi.org/10.1002/2015JC011286, 2016.

Bernardello, R., Marinov, I., Palter, J. B., Galbraith, E. D., and Sarmiento, J. L.: Impact of Weddell Sea deep convection on natural and anthropogenic carbon in a climate model, Geophys. Res. Lett., 41, 7262–7269, https://doi.org/10.1002/2014GL061313, 2014.

Boot, A., van Westen, R. M., and Dijkstra, H. A.: Multidecadal polynya formation in a conceptual (box) model, Ocean Sci., 17, 335–350, https://doi.org/10.5194/os-17-335-2021, 2021.

Bromwich, D. H. and Kurtz, D. D.: Katabatic wind forcing of the Terra Nova Bay polynya, J. Geophys. Res., 89, 3561–3572, https://doi.org/10.1029/JC089iC03p03561, 1984.

Cabré, A., Marinov, I., and Gnanadesikan, A.: Global Atmospheric Teleconnections and Multidecadal Climate Oscillations Driven by Southern Ocean Convection, J. Clim., 30, 8107–8126, https://doi.org/10.1175/JCLI-D-16-0741.1, 2017.

Campbell, E. C., Wilson, E. A., Moore, G. W. K., Riser, S. C., Brayton, C. E., Mazloff, M. R., and Talley, L. D.: Antarctic offshore polynyas linked to Southern Hemisphere climate anomalies, Nature, 570, 319–325, https://doi.org/10.1038/s41586-019-1294-0, 2019.

Carsey, F. D.: Microwave Observation of the Weddell Polynya, Mon. Weather Rev., 108, 2032–2044, https://doi.org/10.1175/1520-0493(1980)108<2032:MOOTWP>2.0.CO;2, 1980.

Casagrande, F., Stachelski, L., and de Souza, R. B.: Assessment of Antarctic sea ice area and concentration in Coupled Model Intercomparison Project Phase 5 and Phase 6 models, Int. J. Climatol., 43, 1314–1332, https://doi.org/10.1002/joc.7916, 2023.

Chang, P., Zhang, S., Danabasoglu, G., Yeager, S. G., Fu, H., Wang, H., Castruccio, F. S., Chen, Y., Edwards, J., Fu, D., Jia, Y., Laurindo, L. C., Liu, X., Rosenbloom, N., Small, R. J., Xu, G., Zeng, Y., Zhang, Q., Bacmeister, J., Bailey, D. A., Duan, X., DuVivier, A. K., Li, D., Li, Y., Neale, R., St"ossel, A., Wang, L., Zhuang, Y., Baker, A., Bates, S., Dennis, J., Diao, X., Gan, B., Gopal, A., Jia, D., Jing, Z., Ma, X., Saravanan, R., Strand, W. G., Tao, J., Yang, H., Wang, X., Wei, Z., and Wu, L.: An Unprecedented Set of High-Resolution Earth System Simulations for Understanding Multiscale Interactions in Climate Variability and Change, J. Adv. Model Earth Syst., 12, e2020MS002 298, https://doi.org/10.1029/2020MS002298, 2020.

https://doi.org/10.5194/egusphere-2026-3060
Preprint. Discussion started: 10 July 2026

Chen, J., Swart, N. C., Beadling, R., Cheng, X., Hattermann, T., Jüling, A., Li, Q., Marshall, J., Martin, T., Muilwijk, M., Pauling, A. G., Purich, A., Smith, I. J., and Thomas, M.: Reduced Deep Convection and Bottom Water Formation Due To Antarctic Meltwater in a Multi-Model Ensemble, Geophys. Res. Lett., 50, e2023GL106 492, https://doi.org/10.1029/2023GL106492, 2023.

Cheon, W. G. and Gordon, A. L.: Open-ocean polynyas and deep convection in the Southern Ocean, Sci. Rep., 9, 1–9, https://doi.org/10.1038/s41598-019-43466-2, 2019.

Cheon, W. G., Park, Y.-G., Toggweiler, J. R., and Lee, S.-K.: The Relationship of Weddell Polynya and Open-Ocean Deep Convection to the Southern Hemisphere Westerlies, J. Phys. Oceanogr., 44, 694–713, https://doi.org/10.1175/JPO-D-13-0112.1, 2014.

Cheon, W. G., Lee, S.-K., Gordon, A. L., Liu, Y., Cho, C.-B., and Park, J. J.: Replicating the 1970s' Weddell Polynya using a coupled ocean-sea ice model with reanalysis surface flux fields, Geophys. Res. Lett., 42, 5411–5418, https://doi.org/10.1002/2015GL064364, 2015.

Comiso, J. C. and Gordon, A. L.: Recurring polynyas over the Cosmonaut Sea and the Maud Rise, J. Geophys. Res. Ocean., 92, 2819–2833, https://doi.org/10.1029/JC092iC03p02819, 1987.

Comiso, J. C. and Gordon, A. L.: Cosmonaut polynya in the Southern Ocean: Structure and variability, J. Geophys. Res. Oceans, 101, 18 297–18 313, https://doi.org/10.1029/96JC01500, 1996.

Comiso, J. C. and Nishio, F.: Trends in the sea ice cover using enhanced and compatible AMSR-E, SSM/I, and SMMR data, J. Geophys. Res. Ocean., 113, https://doi.org/10.1029/2007JC004257, 2008.

Danabasoglu, G., Lamarque, J., Bacmeister, J., Bailey, D. A., DuVivier, A. K., Edwards, J., Emmons, L. K., Fasullo, J., Garcia, R., Gettelman, A., Hannay, C., Holland, M. M., Large, W. G., Lauritzen, P. H., Lawrence, D. M., Lenaerts, J. T. M., Lindsay, K., Lipscomb, W. H., Mills, M. J., Neale, R., Oleson, K. W., Otto-Bliesner, B., Phillips, A. S., Sacks, W., Tilmes, S., Van Kampenhout, L., Vertenstein, M., Bertini, A., Dennis, J., Deser, C., Fischer, C., Fox-Kemper, B., Kay, J. E., Kinnison, D., Kushner, P. J., Larson, V. E., Long, M. C., Mickelson, S., Moore, J. K., Nienhouse, E., Polvani, L., Rasch, P. J., and Strand, W. G.: The Community Earth System Model Version 2 (CESM2), J. Adv. Model Earth Syst., 12, e2019MS001 916, https://doi.org/10.1029/2019MS001916, 2020.

de Boyer Montégut, C., Madec, G., Fischer, A. S., Lazar, A., and Iudicone, D.: Mixed layer depth over the global ocean: An examination of profile data and a profile-based climatology, J. Geophys. Res. Ocean., 109, 1–20, https://doi.org/10.1029/2004JC002378, 2004.

de Lavergne, C., Palter, J. B., Galbraith, E. D., Bernardello, R., and Marinov, I.: Cessation of deep convection in the open Southern Ocean under anthropogenic climate change, Nat. Clim. Chang., 4, 278–282, https://doi.org/10.1038/nclimate2132, 2014.

de Steur, L., Holland, D. M., Muench, R. D., and McPhee, M. G.: The warm-water "Halo" around Maud Rise: Properties, dynamics and Impact, Deep Sea Res. Part I Oceanogr. Res. Pap., 54, 871–896, https://doi.org/10.1016/j.dsr.2007.03.009, 2007.

Diao, X., Stössel, A., Chang, P., Danabasoglu, G., Yeager, S. G., Gopal, A., Wang, H., and Zhang, S.: On the Intermittent Occurrence of Open-Ocean Polynyas in a Multi-Century High-Resolution Preindustrial Earth System Model Simulation, J. Geophys. Res. Ocean., 127, https://doi.org/10.1029/2021JC017672, 2022.

Dufour, C. O., Morrison, A. K., Griffies, S. M., Frenger, I., Zanowski, H., and Winton, M.: Preconditioning of the Weddell Sea Polynya by the Ocean Mesoscale and Dense Water Overflows, J. Clim., 30, 7719–7737, https://doi.org/10.1175/JCLI-D-16-0586.1, 2017.

Dutta, S., Sabu, P., Narayanan, A., and Mohan, R.: Characteristics of an Annually Recurring Open-Ocean Polynya in the Southern Ocean, J. Geophys. Res. Oceans, 131, e2025JC022 821, https://doi.org/10.1029/2025JC022821, 2026.

Eyring, V., Bony, S., Meehl, G. A., Senior, C. A., Stevens, B., Stouffer, R. J., and Taylor, K. E.: Overview of the Coupled Model Intercomparison Project Phase 6 (CMIP6) experimental design and organization, Geosci. Model Dev., 9, 1937–1958, https://doi.org/10.5194/gmd-9-1937-2016, 2016.

https://doi.org/10.5194/egusphere-2026-3060
Preprint. Discussion started: 10 July 2026

Francis, D., Eayrs, C., Cuesta, J., and Holland, D.: Polar Cyclones at the Origin of the Reoccurrence of the Maud Rise Polynya in Austral Winter 2017, J. Geophys. Res. Atmos., 124, 5251–5267, https://doi.org/10.1029/2019JD030618, 2019.

Fusco, G., Budillon, G., and Spezie, G.: Surface heat fluxes and thermohaline variability in the Ross Sea and in Terra Nova Bay polynya, Cont. Shelf Res., 29, 1887–1895, https://doi.org/10.1016/j.csr.2009.07.006, 2009.

Golaz, J., Van Roekel, L. P., Zheng, X., Roberts, A. F., Wolfe, J. D., Lin, W., Bradley, A. M., Tang, Q., Maltrud, M. E., Forsyth, R. M., Zhang, C., Zhou, T., Zhang, K., Zender, C. S., Wu, M., Wang, H., Turner, A. K., Singh, B., Richter, J. H., Qin, Y., Petersen, M. R., Mametjanov, A., Ma, P., Larson, V. E., Krishna, J., Keen, N. D., Jeffery, N., Hunke, E. C., Hannah, W. M., Guba, O., Griffin, B. M., Feng, Y., Engwirda, D., Di Vittorio, A. V., Dang, C., Conlon, L. M., Chen, C., Brunke, M. A., Bisht, G., Benedict, J. J., Asay-Davis, X. S., Zhang, Y., Zhang, M., Zeng, X., Xie, S., Wolfram, P. J., Vo, T., Veneziani, M., Tesfa, T. K., Sreepathi, S., Salinger, A. G., Reeves Eyre, J. E. J., Prather, M. J., Mahajan, S., Li, Q., Jones, P. W., Jacob, R. L., Huebler, G. W., Huang, X., Hillman, B. R., Harrop, B. E., Foucar, J. G., Fang, Y., Comeau, D. S., Caldwell, P. M., Bartoletti, T., Balaguru, K., Taylor, M. A., McCoy, R. B., Leung, L. R., and Bader, D. C.: The DOE E3SM Model Version 2: Overview of the Physical Model and Initial Model Evaluation, J. Adv. Model Earth Syst., 14, e2022MS003 156, https://doi.org/10.1029/2022MS003156, 2022.

Golledge, N. R., Keller, E. D., Gossart, A., Malyarenko, A., Bahamondes-Dominguez, A., Krapp, M., Jendersie, S., Lowry, D. P., Alevropoulos-Borrill, A., and Notz, D.: Antarctic coastal polynyas in the global climate system, Nat. Rev. Earth Environ., 6, 126–139, https://doi.org/10.1038/s43017-024-00634-x, 2025.

Goosse, H. and Fichefet, T.: Open-ocean convection and polynya formation in a large-scale ice–ocean model, Tellus A Dyn. Meteorol. Oceanogr., 53, 94–111, https://doi.org/10.3402/tellusa.v53i1.12175, 2001.

Gordon, A.: Weddell Deep Water variability, J. Mar. Res., 40, https://elischolar.library.yale.edu/journal_of_marine_research/1640, 1982.

Gordon, A. L.: Deep Antarctic Convection West of Maud Rise, J. Phys. Oceanogr., 8, 600–612, https://doi.org/10.1175/1520-0485(1978)008<0600:DACWOM>2.0.CO;2, 1978.

Gordon, A. L., Visbeck, M., and Comiso, J. C.: A Possible Link between the Weddell Polynya and the Southern Annular Mode, J. Clim., 20, 2558–2571, https://doi.org/10.1175/JCLI4046.1, 2007.

Griffies, S. M., Danabasoglu, G., Durack, P. J., Adcroft, A. J., Balaji, V., Böning, C. W., Chassignet, E. P., Curchitser, E., Deshayes, J., Drange, H., Fox-Kemper, B., Gleckler, P. J., Gregory, J. M., Haak, H., Hallberg, R. W., Heimbach, P., Hewitt, H. T., Holland, D. M., Ilyina, T., Jungclaus, J. H., Komuro, Y., Krasting, J. P., Large, W. G., Marsland, S. J., Masina, S., McDougall, T. J., Nurser, A. J. G., Orr, J. C., Pirani, A., Qiao, F., Stouffer, R. J., Taylor, K. E., Treguier, A. M., Tsujino, H., Uotila, P., Valdivieso, M., Wang, Q., Winton, M., and Yeager, S. G.: OMIP contribution to CMIP6: experimental and diagnostic protocol for the physical component of the Ocean Model Intercomparison Project, Geosci. Model Dev., 9, 3231–3296, https://doi.org/10.5194/gmd-9-3231-2016, 2016.

Griffies, S. M., Adcroft, A., and Hallberg, R. W.: A Primer on the Vertical Lagrangian-Remap Method in Ocean Models Based on Finite Volume Generalized Vertical Coordinates, JAMES, 12, e2019MS001 954, https://doi.org/10.1029/2019MS001954, 2020.

Gutjahr, O., Brüggemann, N., Haak, H., Jungclaus, J. H., Putrasahan, D. A., Lohmann, K., and Von Storch, J.-S.: Comparison of ocean vertical mixing schemes in the Max Planck Institute Earth System Model (MPI-ESM1.2), Geosci. Model Dev., 14, 2317–2349, https://doi.org/10.5194/gmd-14-2317-2021, 2021.

Haid, V. and Timmermann, R.: Simulated heat flux and sea ice production at coastal polynyas in the southwestern Weddell Sea, J. Geophys. Res. Ocean., 118, 2640–2652, https://doi.org/10.1002/jgrc.20133, 2013.

Held, I. M., Guo, H., Adcroft, A., Dunne, J. P., Horowitz, L. W., Krasting, J., Shevliakova, E., Winton, M., Zhao, M., Bushuk, M., Wittenberg, A. T., Wyman, B., Xiang, B., Zhang, R., Anderson, W., Balaji, V., Donner, L., Dunne, K., Durachta, J., Gauthier, P. P. G.,

https://doi.org/10.5194/egusphere-2026-3060
Preprint. Discussion started: 10 July 2026

Ginoux, P., Golaz, J., Griffies, S. M., Hallberg, R., Harris, L., Harrison, M., Hurlin, W., John, J., Lin, P., Lin, S., Malyshev, S., Menzel, R., Milly, P. C. D., Ming, Y., Naik, V., Paynter, D., Paulot, F., Ramaswamy, V., Reichl, B., Robinson, T., Rosati, A., Seman, C., Silvers, L. G., Underwood, S., and Zadeh, N.: Structure and Performance of GFDL's CM4.0 Climate Model, JAMES, 11, 3691–3727, https://doi.org/10.1029/2019MS001829, 2019.

Heuzé, C.: Antarctic Bottom Water and North Atlantic Deep Water in CMIP6 models, Ocean Sci., 17, 59–90, https://doi.org/10.5194/os-17-59-2021, 2021.

Heuzé, C., Heywood, K. J., Stevens, D. P., and Ridley, J. K.: Southern Ocean bottom water characteristics in CMIP5 models, Geophys. Res. Lett., 40, 1409–1414, https://doi.org/10.1002/grl.50287, 2013.

Heuzé, C., Ridley, J. K., Calvert, D., Stevens, D. P., and Heywood, K. J.: Increasing vertical mixing to reduce Southern Ocean deep convection in NEMO3.4, Geosci. Model Dev., 8, 3119–3130, https://doi.org/10.5194/gmd-8-3119-2015, 2015.

Holland, D. M.: Explaining the Weddell Polynya–a Large Ocean Eddy Shed at Maud Rise, Science, 292, 1697–1700, https://doi.org/10.1126/science.1059322, 2001.

Huot, P.-V., Kittel, C., Fichefet, T., Jourdain, N. C., Sterlin, J., and Fettweis, X.: Effects of the atmospheric forcing resolution on simulated sea ice and polynyas off Adélie Land, East Antarctica, Ocean Model., 168, 101 901, https://doi.org/10.1016/j.ocemod.2021.101901, 2021.

Jena, B., Ravichandran, M., and Turner, J.: Recent Reoccurrence of Large Open-Ocean Polynya on the Maud Rise Seamount, Geophys. Res. Lett., 46, 4320–4329, https://doi.org/10.1029/2018GL081482, 2019.

Jeong, H., Asay-Davis, X. S., Turner, A. K., Comeau, D. S., Price, S. F., Abernathey, R. P., Veneziani, M., Petersen, M. R., Hoffman, M. J., Mazloff, M. R., and Ringler, T. D.: Impacts of Ice-Shelf Melting on Water-Mass Transformation in the Southern Ocean from E3SM Simulations, J. Clim., 33, 5787–5807, https://doi.org/10.1175/JCLI-D-19-0683.1, 2020.

Jeong, H., Turner, A. K., Roberts, A. F., Veneziani, M., Price, S. F., Asay-Davis, X. S., Van Roekel, L. P., Lin, W., Caldwell, P. M., Park, H.-S., Wolfe, J. D., and Mametjanov, A.: Southern Ocean polynyas and dense water formation in a high-resolution, coupled Earth system model, Cryosph., 17, 2681–2700, https://doi.org/10.5194/tc-17-2681-2023, 2023.

Kaufman, Z. S., Feldl, N., Weijer, W., and Veneziani, M.: Causal Interactions between Southern Ocean Polynyas and High-Latitude Atmosphere–Ocean Variability, J. Clim., 33, 4891–4905, https://doi.org/10.1175/JCLI-D-19-0525.1, 2020.

Kern, S., Spreen, G., Kaleschke, L., De La Rosa, S., and Heygster, G.: Polynya Signature Simulation Method polynya area in comparison to AMSR-E 89GHz sea-ice concentrations in the Ross Sea and off the Adélie Coast, Antarctica, for 2002–05: first results, Ann. Glaciol., 46, 409–418, https://doi.org/10.3189/172756407782871585, 2007.

Kurtakoti, P., Veneziani, M., Stössel, A., and Weijer, W.: Preconditioning and Formation of Maud Rise Polynyas in a High-Resolution Earth System Model, J. Clim., 31, 9659–9678, https://doi.org/10.1175/JCLI-D-18-0392.1, 2018.

Landrum, L. L., DuVivier, A. K., Holland, M. M., Krumhardt, K., and Sylvester, Z.: Challenges in identifying Antarctic coastal polynyas in satellite observations and climate model output to support ecological climate change research, The Cryosphere, 20, 1815–1840, https://doi.org/10.5194/tc-20-1815-2026, 2026.

Latif, M., Martin, T., and Park, W.: Southern Ocean Sector Centennial Climate Variability and Recent Decadal Trends, J. Clim., 26, 7767–7782, https://doi.org/10.1175/JCLI-D-12-00281.1, 2013.

Li, Q., England, M. H., Hogg, A. M., Rintoul, S. R., and Morrison, A. K.: Abyssal ocean overturning slowdown and warming driven by Antarctic meltwater, Nature, 615, 841–847, https://doi.org/10.1038/s41586-023-05762-w, 2023.

Li, S., Huang, G., Li, X., Liu, J., and Fan, G.: An Assessment of the Antarctic Sea Ice Mass Budget Simulation in CMIP6 Historical Experiment, Front. Earth Sci., 9, 1–17, https://doi.org/10.3389/feart.2021.649743, 2021.

https://doi.org/10.5194/egusphere-2026-3060
Preprint. Discussion started: 10 July 2026

Lin, P., Yu, Z., Liu, H., Yu, Y., Li, Y., Jiang, J., Xue, W., Chen, K., Yang, Q., Zhao, B., Wei, J., Ding, M., Sun, Z., Wang, Y., Meng, Y., Zheng, W., and Ma, J.: LICOM Model Datasets for the CMIP6 Ocean Model Intercomparison Project, Adv. Atmos. Sci., 37, 239–249, https://doi.org/10.1007/s00376-019-9208-5, 2020.

Liu, G., Tagklis, F., Ito, T., and Bracco, A.: Drivers of coupled climate model biases in representing Labrador Sea convection, Clim. Dyn., 62, 3337–3353, https://doi.org/10.1007/s00382-023-07068-z, 2024.

Liu, H., Lin, P., Yu, Y., and Zhang, X.: The baseline evaluation of LASG/IAP climate system ocean model (LICOM) version 2, Acta Meteorol. Sin., 26, 318–329, https://doi.org/10.1007/s13351-012-0305-y, 2012.

Martin, T., Park, W., and Latif, M.: Multi-centennial variability controlled by Southern Ocean convection in the Kiel Climate Model, Clim. Dyn., 40, 2005–2022, https://doi.org/10.1007/s00382-012-1586-7, 2013.

Massom, R. A., Harris, P., Michael, K. J., and Potter, M.: The distribution and formative processes of latent-heat polynyas in East Antarctica, Ann. Glaciol., 27, 420–426, https://doi.org/10.3189/1998AoG27-1-420-426, 1998.

McDougall, T. J., Barker, P. M., Holmes, R. M., Pawlowicz, R., Griffies, S. M., and Durack, P. J.: The interpretation of temperature and salinity variables in numerical ocean model output and the calculation of heat fluxes and heat content, Geosci. Model Dev., 14, 6445–6466, https://doi.org/10.5194/gmd-14-6445-2021, 2021.

Mohrmann, M., Heuzé, C., and Swart, S.: Southern Ocean polynyas in CMIP6 models, Cryosph., 15, 4281–4313, https://doi.org/10.5194/tc-15-4281-2021, 2021.

Morales Maqueda, M. A., Willmott, A. J., and Biggs, N. R. T.: Polynya Dynamics: a Review of Observations and Modeling, Rev. Geophys., 42, https://doi.org/10.1029/2002RG000116, 2004.

Narayanan, A., Roquet, F., Gille, S. T., Gülk, B., Mazloff, M. R., Silvano, A., and Naveira Garabato, A. C.: Ekman-Driven Salt Transport as a Key Mechanism for Open-Ocean Polynya Formation at Maud Rise, Sci. Adv., 10, eadj0777, https://doi.org/10.1126/sciadv.adj0777, 2024.

Nie, Y., Lin, X., Yang, Q., Liu, J., Chen, D., and Uotila, P.: Differences Between the CMIP5 and CMIP6 Antarctic Sea Ice Concentration Budgets, Geophys. Res. Lett., 50, https://doi.org/10.1029/2023GL105265, 2023.

Notz, D., Jahn, A., Holland, M., Hunke, E., Massonnet, F., Stroeve, J., Tremblay, B., and Vancoppenolle, M.: The CMIP6 Sea-Ice Model Intercomparison Project (SIMIP): understanding sea ice through climate-model simulations, Geosci. Model Dev., 9, 3427–3446, https://doi.org/10.5194/gmd-9-3427-2016, 2016.

Ohshima, K. I., Fukamachi, Y., Williams, G. D., Nihashi, S., Roquet, F., Kitade, Y., Tamura, T., Hirano, D., Herraiz-Borreguero, L., Field, I., Hindell, M., Aoki, S., and Wakatsuchi, M.: Antarctic Bottom Water production by intense sea-ice formation in the Cape Darnley polynya, Nat. Geosci., 6, 235–240, https://doi.org/10.1038/ngeo1738, 2013.

Ohshima, K. I., Nihashi, S., and Iwamoto, K.: Global view of sea-ice production in polynyas and its linkage to dense/bottom water formation, Geosci. Lett., 3, 13, https://doi.org/10.1186/s40562-016-0045-4, 2016.

Ohshima, K. I., Fukamachi, Y., Ito, M., Nakata, K., Simizu, D., Ono, K., Nomura, D., Hashida, G., and Tamura, T.: Dominant frazil ice production in the Cape Darnley polynya leading to Antarctic Bottom Water formation, Sci. Adv., 8, eadc9174, https://doi.org/10.1126/sciadv.adc9174, 2022.

Parkinson, C. L.: On the Development and Cause of the Weddell Polynya in a Sea Ice Simulation, J. Phys. Oceanogr., 13, 501–511, https://doi.org/10.1175/1520-0485(1983)013<0501:OTDACO>2.0.CO;2, 1983.

Reintges, A., Martin, T., Latif, M., and Park, W.: Physical controls of Southern Ocean deep-convection variability in CMIP5 models and the Kiel Climate Model, Geophys. Res. Lett., 44, 6951–6958, https://doi.org/10.1002/2017GL074087, 2017.

https://doi.org/10.5194/egusphere-2026-3060
Preprint. Discussion started: 10 July 2026

Rheinlænder, J. W., Smedsrud, L. H., and Nisanciouglu, K. H.: Internal Ocean Dynamics Control the Long-Term Evolution of Weddell Sea Polynya Activity, Front. Clim., 3, 718 016, https://doi.org/10.3389/fclim.2021.718016, 2021.

Ringler, T., Petersen, M., Higdon, R. L., Jacobsen, D., Jones, P. W., and Maltrud, M.: A multi-resolution approach to global ocean modeling, Ocean Modell., 69, 211–232, https://doi.org/10.1016/j.ocemod.2013.04.010, 2013.

Roach, L. A., Dörr, J., Holmes, C. R., Massonnet, F., Blockley, E. W., Notz, D., Rackow, T., Raphael, M. N., O'Farrell, S. P., Bailey, D. A., and Bitz, C. M.: Antarctic Sea Ice Area in CMIP6, Geophys. Res. Lett., 47, 1–10, https://doi.org/10.1029/2019GL086729, 2020.

Seland, Ø., Bentsen, M., Olivié, D., Toniazzo, T., Gjermundsen, A., Graff, L. S., Debernard, J. B., Gupta, A. K., He, Y.-C., Kirkevåg, A., Schwinger, J., Tjiputra, J., Aas, K. S., Bethke, I., Fan, Y., Griesfeller, J., Grini, A., Guo, C., Ilicak, M., Karset, I. H. H., Landgren, O., Liakka, J., Moseid, K. O., Nummelin, A., Spensberger, C., Tang, H., Zhang, Z., Heinze, C., Iversen, T., and Schulz, M.: Overview of the Norwegian Earth System Model (NorESM2) and key climate response of CMIP6 DECK, historical, and scenario simulations, Geosci. Model Dev., 13, 6165–6200, https://doi.org/10.5194/gmd-13-6165-2020, 2020.

Seroussi, H., Nowicki, S., Payne, A. J., Goelzer, H., Lipscomb, W. H., Abe-Ouchi, A., Agosta, C., Albrecht, T., Asay-Davis, X., Barthel, A., Calov, R., Cullather, R., Dumas, C., Galton-Fenzi, B. K., Gladstone, R., Golledge, N. R., Gregory, J. M., Greve, R., Hattermann, T., Hoffman, M. J., Humbert, A., Huybrechts, P., Jourdain, N. C., Kleiner, T., Larour, E., Leguy, G. R., Lowry, D. P., Little, C. M., Morlighem, M., Pattyn, F., Pelle, T., Price, S. F., Quiquet, A., Reese, R., Schlegel, N.-J., Shepherd, A., Simon, E., Smith, R. S., Straneo, F., Sun, S., Trusel, L. D., Van Breedam, J., Van De Wal, R. S. W., Winkelmann, R., Zhao, C., Zhang, T., and Zwinger, T.: ISMIP6 Antarctica: a multi-model ensemble of the Antarctic ice sheet evolution over the 21st century, The Cryosphere, 14, 3033–3070, https://doi.org/10.5194/tc-14-3033-2020, 2020.

Shu, Q., Wang, Q., Song, Z., Qiao, F., Zhao, J., Chu, M., and Li, X.: Assessment of Sea Ice Extent in CMIP6 With Comparison to Observations and CMIP5, Geophys. Res. Lett., 47, 1–9, https://doi.org/10.1029/2020GL087965, 2020.

Silvano, A., Purkey, S., Gordon, A. L., Castagno, P., Stewart, A. L., Rintoul, S. R., Foppert, A., Gunn, K. L., Herraiz-Borreguero, L., Aoki, S., Nakayama, Y., Naveira Garabato, A. C., Spingys, C., Akhoudas, C. H., Sallée, J.-B., De Lavergne, C., Abrahamsen, E. P., Meijers, A. J. S., Meredith, M. P., Zhou, S., Tamura, T., Yamazaki, K., Ohshima, K. I., Falco, P., Budillon, G., Hattermann, T., Janout, M. A., Llanillo, P., Bowen, M. M., Darelius, E., Østerhus, S., Nicholls, K. W., Stevens, C., Fernandez, D., Cimoli, L., Jacobs, S. S., Morrison, A. K., Hogg, A. M., Haumann, F. A., Mashayek, A., Wang, Z., Kerr, R., Williams, G. D., and Lee, W. S.: Observing Antarctic Bottom Water in the Southern Ocean, Front. Mar. Sci., 10, 1221 701, https://doi.org/10.3389/fmars.2023.1221701, 2023.

Smedsrud, L. H.: Warming of the deep water in the Weddell Sea along the Greenwich meridian: 1977–2001, Deep Sea Res. Part I Oceanogr. Res. Pap., 52, 241–258, https://doi.org/10.1016/j.dsr.2004.10.004, 2005.

Tamura, T., Ohshima, K. I., and Nihashi, S.: Mapping of sea ice production for Antarctic coastal polynyas, Geophys. Res. Lett., 35, 1–5, https://doi.org/10.1029/2007GL032903, 2008.

Tatebe, H., Ogura, T., Nitta, T., Komuro, Y., Ogochi, K., Takemura, T., Sudo, K., Sekiguchi, M., Abe, M., Saito, F., Chikira, M., Watanabe, S., Mori, M., Hirota, N., Kawatani, Y., Mochizuki, T., Yoshimura, K., Takata, K., O'ishi, R., Yamazaki, D., Suzuki, T., Kurogi, M., Kataoka, T., Watanabe, M., and Kimoto, M.: Description and basic evaluation of simulated mean state, internal variability, and climate sensitivity in MIROC6, Geosci. Model Dev., 12, 2727–2765, https://doi.org/10.5194/gmd-12-2727-2019, 2019.

Tesdal, J., MacGilchrist, G. A., Beadling, R. L., Griffies, S. M., Krasting, J. P., and Durack, P. J.: Revisiting Interior Water Mass Responses to Surface Forcing Changes and the Subsequent Effects on Overturning in the Southern Ocean, J. Geophys. Res. Ocean., 128, https://doi.org/10.1029/2022JC019105, 2023.

https://doi.org/10.5194/egusphere-2026-3060
Preprint. Discussion started: 10 July 2026

Thompson, L., Smith, M., Thomson, J., Stammerjohn, S., Ackley, S., and Loose, B.: Frazil ice growth and production during katabatic wind events in the Ross Sea, Antarctica, Cryosph., 14, 3329–3347, https://doi.org/10.5194/tc-14-3329-2020, 2020.

Tschudi, M. A., Meier, W. N., and Stewart, J. S.: An enhancement to sea ice motion and age products at the National Snow and Ice Data Center (NSIDC), Cryosph., 14, 1519–1536, https://doi.org/10.5194/tc-14-1519-2020, 2020.

Uotila, P., Iovino, D., Vancoppenolle, M., Lensu, M., and Rousset, C.: Comparing sea ice, hydrography and circulation between NEMO3.6 LIM3 and LIM2, Geosci. Model Dev., 10, 1009–1031, https://doi.org/10.5194/gmd-10-1009-2017, 2017.

Weijer, W., Veneziani, M., Stössel, A., Hecht, M. W., Jeffery, N., Jonko, A., Hodos, T., and Wang, H.: Local Atmospheric Response to an Open-Ocean Polynya in a High-Resolution Climate Model, J. Clim., 30, 1629–1641, https://doi.org/10.1175/JCLI-D-16-0120.1, 2017.

Zanowski, H., Hallberg, R., and Sarmiento, J. L.: Abyssal Ocean Warming and Salinification after Weddell Polynyas in the GFDL CM2G Coupled Climate Model, J. Phys. Oceanogr., 45, 2755–2772, https://doi.org/10.1175/JPO-D-15-0109.1, 2015.

Zeller, M. and Martin, T.: On warm bias and mesoscale dynamics setting the Southern Ocean large-scale circulation mean state, Ocean Modell., 191, 102 426, https://doi.org/10.1016/j.ocemod.2024.102426, 2024.

Zhang, L., Delworth, T. L., Cooke, W., and Yang, X.: Natural variability of Southern Ocean convection as a driver of observed climate trends, Nat. Clim. Change, 9, 59–65, https://doi.org/10.1038/s41558-018-0350-3, 2019.

Zhou, L., Ayres, H., Gülk, B., Narayanan, A., De Lavergne, C., Ödalen, M., Silvano, A., Wang, X., Lindeman, M., and Steiger, N.: Review article: Weddell Sea Polynya formation, cessation and climatic impacts, The Cryosphere, 20, 285–308, https://doi.org/10.5194/tc-20-285-2026, 2026.

https://doi.org/10.5194/egusphere-2026-3060
Preprint. Discussion started: 10 July 2026

Table 1. CMIP6 models included in this study.

	model name	ocean module	ice module	resolution (horizotal, vertical)
1	BCC-CSM2-MR	MOM4-L40v2	SISv2	360 x 232, 40
2	BCC-ESM1	MOM4-L40v2	SISv2	360 x 232, 40
3	CAMS-CSM1-0	MOM4	SIS1.0	360 x 200, 50
4	ACCESS-ESM1-5	MOM5	CICE4.1	360 x 300, 50
5	ACCESS-CM2	MOM5	CICE5.1.2	360 x 300 , 50
6	GFDL-CM4	MOM6	SIS2.0	1440 x 1080, 75
7	GFDL-ESM4	MOM6	SIS2.0	720 x 576, 75
8	INM-CM4-8	INM-OM5	INM-ICE1	360 x 318, 40
9	SAM0-UNICON	POP2	CICE4.0	320 x 384, 60
10	CIESM	POP2	CICE4.1	720 x 560, 46
11	CESM2	POP2.1	CICE5.1.2	320 x 384, 60
12	CESM2-FV2	POP2.1	CICE5.1.2	320 x 384, 60
13	CESM2-WACCM	POP2.1	CICE5.1.2	320 x 384, 60
14	CESM2-WACCM-FV2	POP2.1	CICE5.1.2	320 x 384, 60
15	CAS-ESM2-0	LICOM2.0	CICE4	362 x 196, 30
16	FGOALS-g3	LICOM3.0	CICE4	360 x 218, 30
17	NESM3	NEMO3.4	CICE4.1	384 x 362, 46
18	CanESM5	NEMO3.4.1	LIM2	361 x 290, 45
19	CanESM5-1	NEMO3.4.1	LIM2	361 x 290, 45
20	CanESM5-CanOE	NEMO3.4.1	LIM2	361 x 290, 45
21	HadGEM3-GC31-LL	NEMO-HadGEM3-GO6.0	CICE-HadGEM3-GSI8	360 x 330, 75
22	HadGEM3-GC31-MM	NEMO-HadGEM3-GO6.0	CICE-HadGEM3-GSI8	1,440 x 1,205, 75
23	UKESM1-0-LL	NEMO-HadGEM3-GO6.0	CICE-HadGEM3-GSI8	360 x 330, 75
24	UKESM1-1-LL	NEMO-HadGEM3-GO6.0	CICE-HadGEM3-GSI8	360 x 330, 75
25	EC-Earth3	NEMO3.6	LIM3	362 x 292 , 75
26	EC-Earth3-CC	NEMO3.6	LIM3	362 x 292 , 75
27	EC-Earth3-Veg	NEMO3.6	LIM3	362 x 292 , 75
28	EC-Earth3-Veg-LR	NEMO3.6	LIM3	362 x 292 , 75
29	EC-Earth3-AerChem	NEMO3.6	LIM3	362 x 292 , 75

https://doi.org/10.5194/egusphere-2026-3060
Preprint. Discussion started: 10 July 2026

Table 1 continued from previous page

	model name	ocean module	ice module	resolution (horizotal, vertical)
30	CNRM-CM6-1	NEMO3.6	GELATO6	362 x 294, 75
31	CNRM-CM6-1-HR	NEMO3.6	GELATO6	1442 x 1050, 75
32	CNRM-ESM2-1	NEMO3.6	GELATO6	362 x 294, 75
33	CMCC-CM2-SR5	NEMO3.6	CICE4	362 x 292, 50
34	CMCC-ESM2	NEMO3.6	CICE4	362 x 292, 50
35	IPSL-CM6A-LR	NEMO3.6	LIM3.6	362 x 332, 75
36	IPSL-CM6A-MR1	NEMO3.6	LIM3.6	362 x 332, 75
37	GISS-E2-1-H	HYCOM	GISS SI	360 x 180, 32
38	E3SM-1-0	MPAS-Ocean6.0	MPAS-Seaice6.0	235160 cells, 60
39	E3SM-2-0	MPAS-Ocean(E3SMv2.0)	MPAS-Seaice (E3SMv2.0)	236853 cells, 60
40	E3SM-2-0-NARRM	MPAS-Ocean(E3SMv2.0)	MPAS-Seaice (E3SMv2.0)	236853 cells, 60
41	NorCPM1	BLOM	CICE4	320 x 384, 53
42	NorESM2-MM	BLOM	CICE5.1.2	360 x 384, 70
43	NorESM2-LM	BLOM	CICE5.1.2	360 x 384, 70
44	MPI-ESM-1-2-HAM	MPIOM1.63	MPI Sea Ice	256 x 220, 40
45	MPI-ESM1-2-HR	MPIOM1.63	MPI Sea Ice	820 x 404, 40
46	MPI-ESM1-2-LR	MPIOM1.63	MPI Sea Ice	256 x 220, 40
47	MIROC6	COCO4.9	COCO4.9	360 x 256, 63
48	MIROC-ES2L	COCO4.9	COCO4.9	360 x 256, 63
49	MIROC-ES2H	COCO4.9	COCO4.9	360 x 256, 63

https://doi.org/10.5194/egusphere-2026-3060
Preprint. Discussion started: 10 July 2026

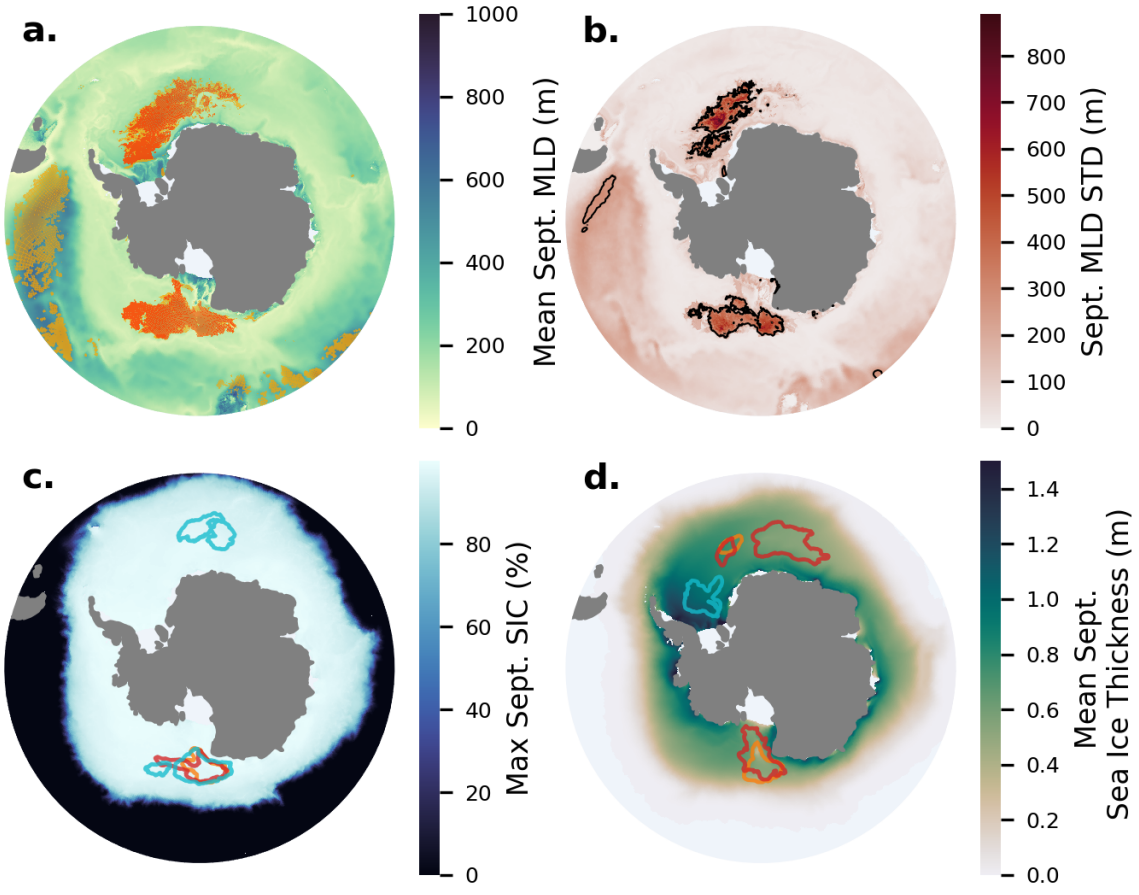

Figure 1. Illustration of deep convection and polynya detection methods, using GFDL-CM4 output as an example. **a.** Deep convection regions identified from September mixed-layer depth (MLD). Background shading (green–blue colormap) is the mean September MLD over the 500-year simulation. Regions where the MLD exceeds 1000 m (2000 m) at least once are highlighted in yellow (orange). **b.** Deep convection regions based on the temporal standard deviation of MLD (STD). The background shading represents the temporal STD of September MLD. Black contours enclose regions where the z-score of STD exceeds 2, indicating areas of anomalously high MLD variability. **c.** Polynya detection using September SIC thresholds. Background shading is the maximum September SIC. Colored contours correspond to different SIC thresholds used to define polynyas: orange (15%), red (45%), and cyan (75%). **d.** Polynya regions identified using September sea ice thickness thresholds. The background shading shows the mean September sea ice thickness. Colored contours denote polynya regions based on different sea ice thickness thresholds: orange (0.2 m), red (0.5 m), and cyan (0.8 m)

https://doi.org/10.5194/egusphere-2026-3060
Preprint. Discussion started: 10 July 2026

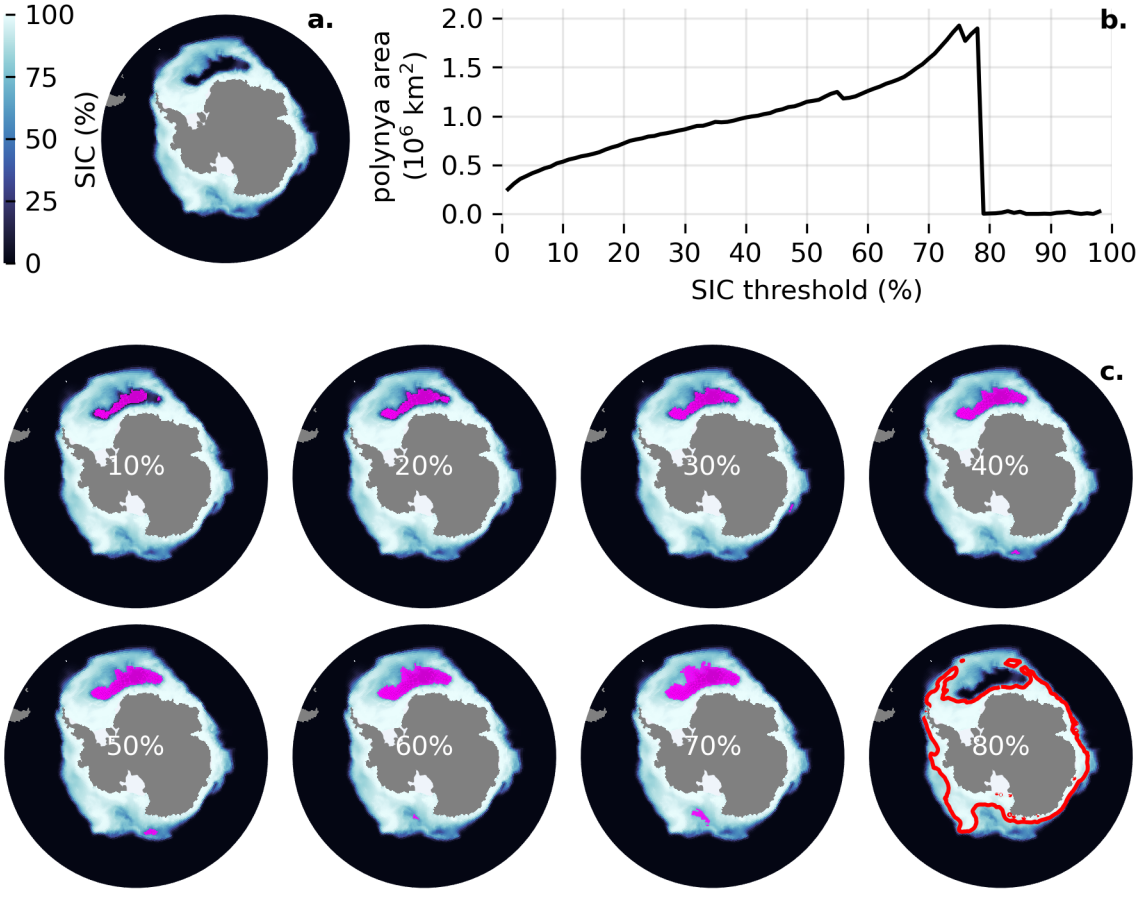

Figure 2. Identification of OOPs in the NorESM2-MM model during model year 1388 using varying SIC thresholds. **a.** September SIC distribution in the SO. **b.** Detected polynya areas changing with the corresponding SIC threshold. **c.** Maps showing OOP detection using SIC thresholds ranging from 10% to 80%. Cyan shading highlights the locations of the detected OOPs; threshold values are labeled at the center of each map. In the map with an 80% threshold, the red contour line denotes the SIC boundary at 80%.

https://doi.org/10.5194/egusphere-2026-3060
Preprint. Discussion started: 10 July 2026

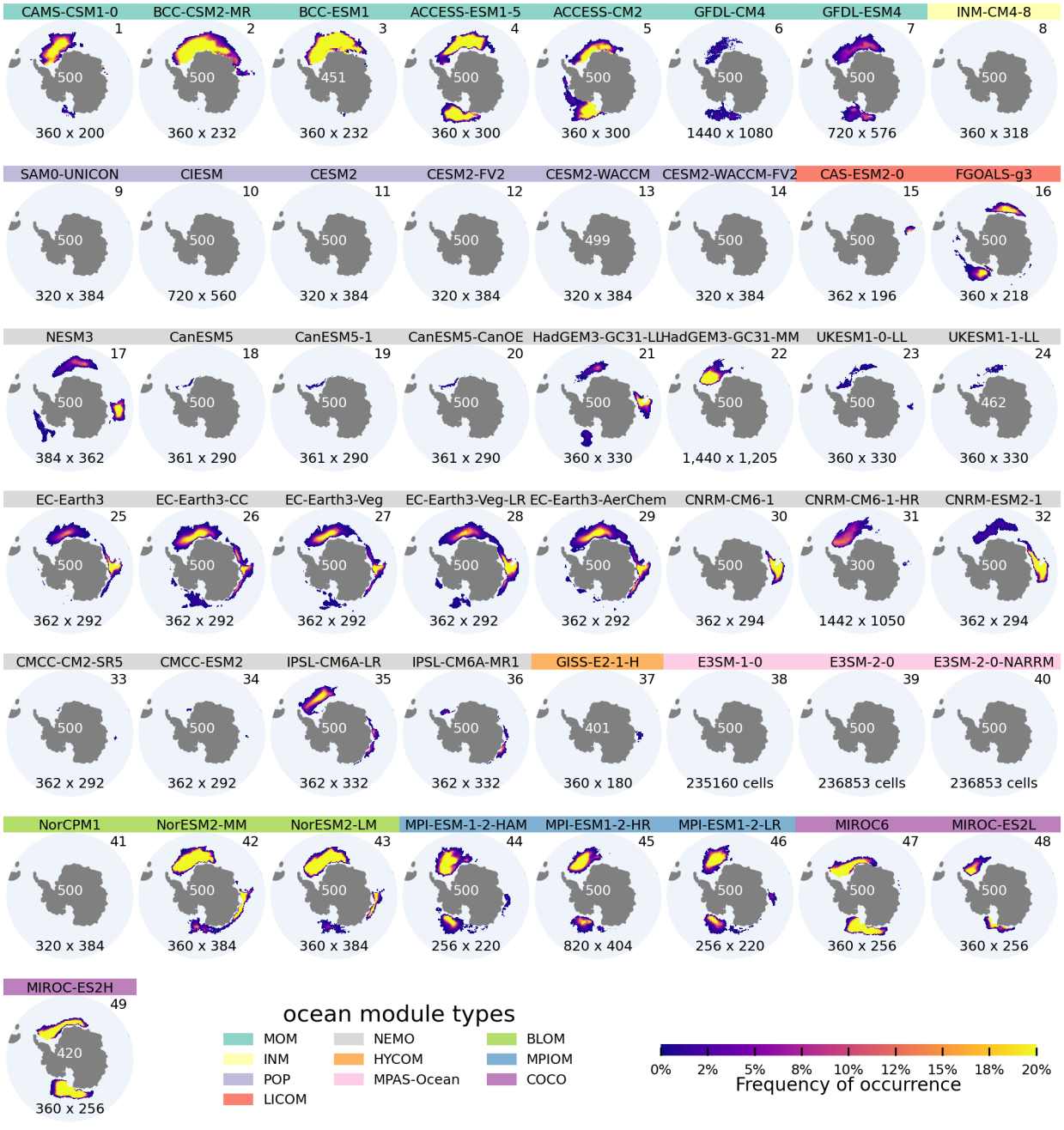

Figure 3. Locations of deep convection regions across CMIP6 models. Color shading indicates the frequency of deep convection occurrence, defined as locations when the September MLD exceeds 2000 m during any year within the analyzed piControl simulation. Yellow indicates more frequent convective events. Total run duration (in years) is shown as white numbers at the center of each map; most model runs are 500 years. Black numbers at the bottom of each map indicate the horizontal resolution of each model. Black numbers at the top right of each map correspond to model numbers, as listed also in Table 1. The background color behind each model name represents its ocean module family groups, as described in Table 1.

https://doi.org/10.5194/egusphere-2026-3060
Preprint. Discussion started: 10 July 2026

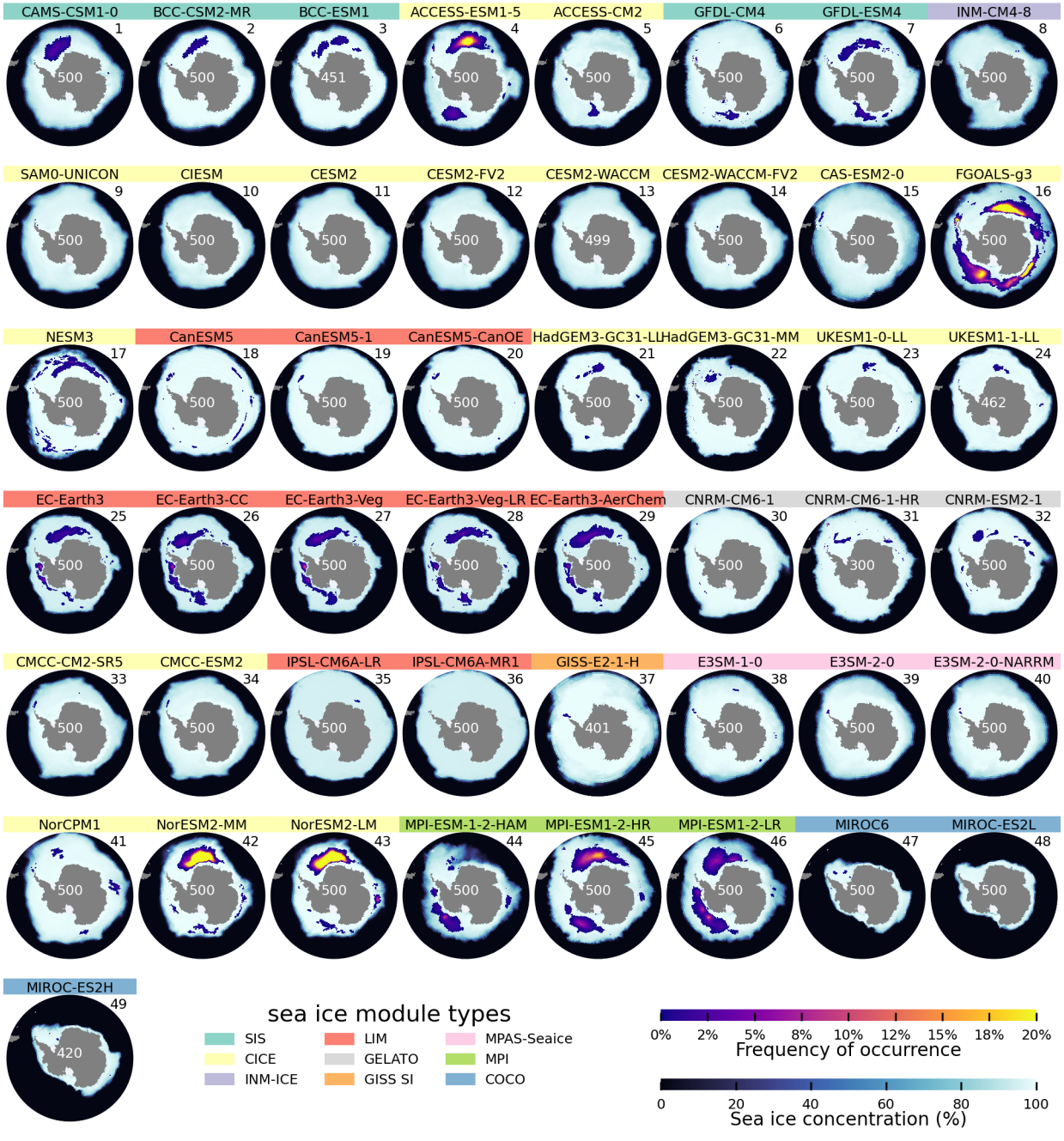

Figure 4. Locations of OOPs across CMIP6 models. Blue to white shading indicates the maximum September SIC across all years, with the white numbers in the middle of each map denoting the number of years analyzed. Purple to yellow shading represents the frequency of OOP occurrences in September, identified using a threshold based on the average SIC within the sea ice extent for each model. Black numbers at the top right of each map correspond to model numbers, as listed in 1. Model names are displayed above each map, with background colors denoting the corresponding sea ice module family, as described in Table 1.

https://doi.org/10.5194/egusphere-2026-3060
Preprint. Discussion started: 10 July 2026

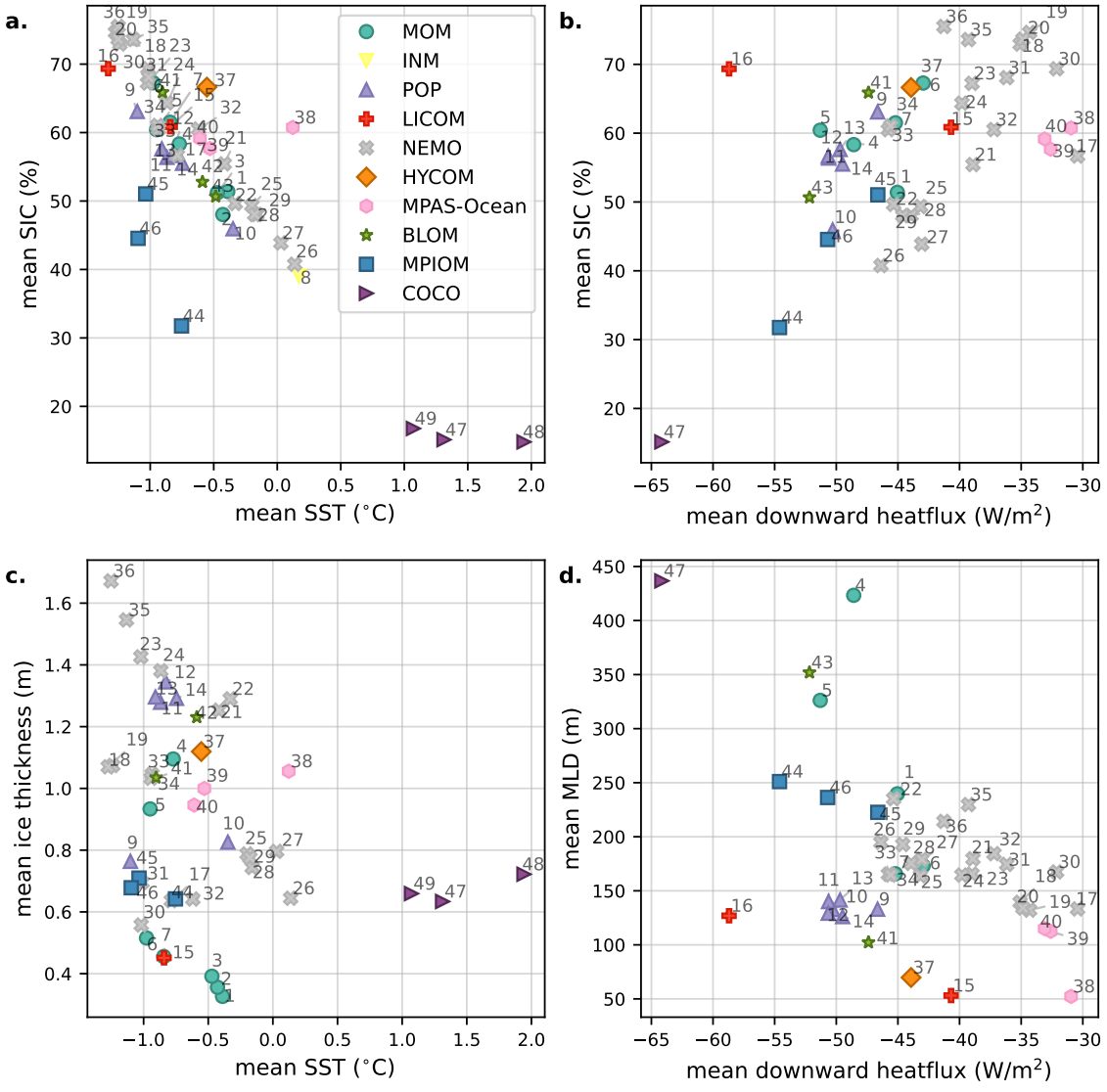

Figure 5. Inter-model relationships of key ocean–ice variables. **a.** SIC (in %) against SST. **b.** SIC against downward surface heat flux. **c.** Sea ice thickness against SST. **d.** MLD against downward surface heat flux. All variables are computed as September averages south of 55°S over the entire available simulation period.

https://doi.org/10.5194/egusphere-2026-3060
Preprint. Discussion started: 10 July 2026

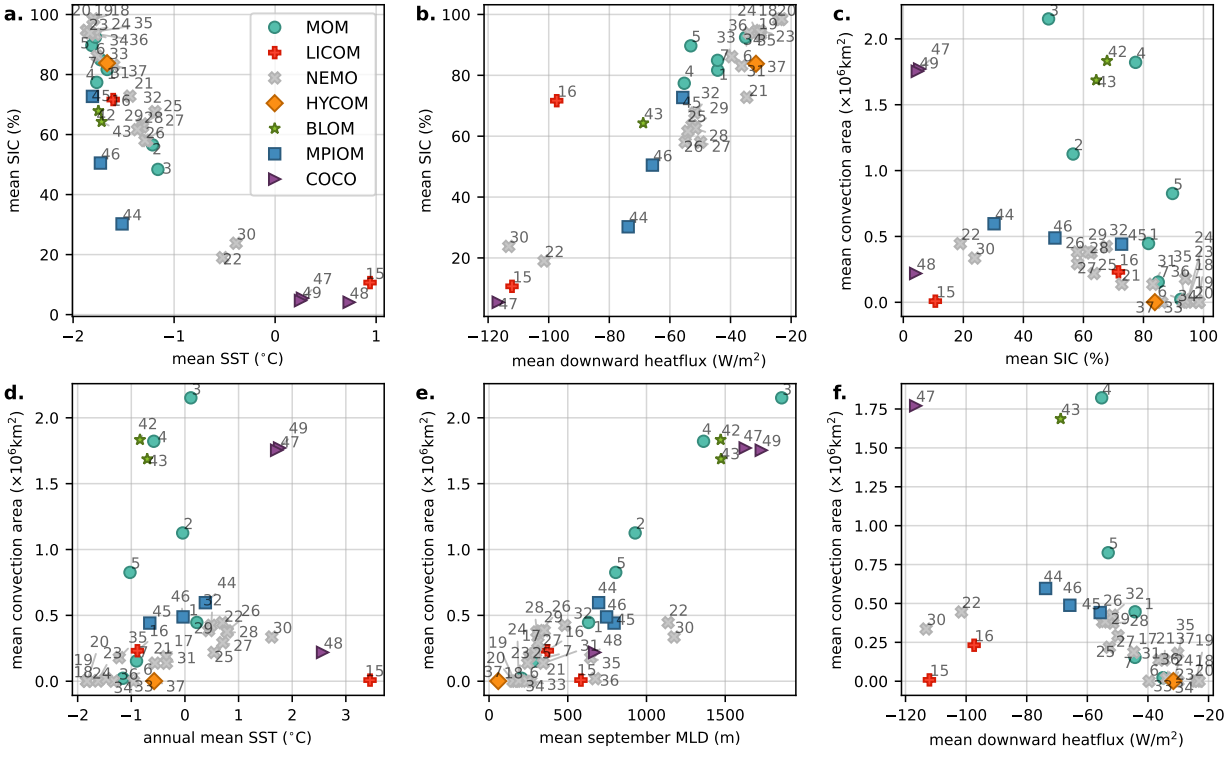

Figure 6. Dynamics inside deep convection areas across models. Unless otherwise specified, all variables are time and space averaged averaged inside each model's total convective area (mapped in Figure 3) and for the month of September: **a.** Mean SIC (%) vs. mean SST (°C). **b.** mean SIC (%) vs downward surface Heat Flux. **c.** SIC south of 55S vs. mean Convective Area. In the bottom row mean convective area is plotted against: **d.** annual mean SST, **e.** mean MLD, **f.** downward surface Heat Flux.

https://doi.org/10.5194/egusphere-2026-3060
Preprint. Discussion started: 10 July 2026

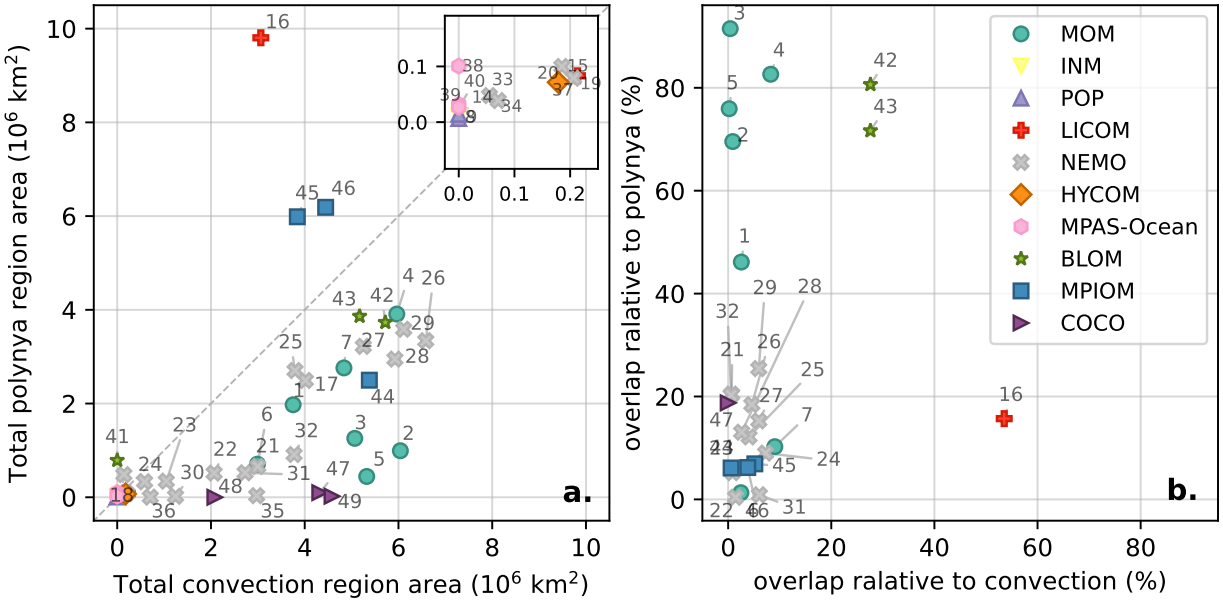

Figure 7. Comparison between OOP areas and deep convection areas. **a.** Total OOP area versus total deep convection area. The dotted 1:1 line is included for reference. **b.** Overlap area expressed as a percentage of the area of all deep convection events (x-axis) versus the percentage of the the area of all OOP events (y-axis).

https://doi.org/10.5194/egusphere-2026-3060
Preprint. Discussion started: 10 July 2026

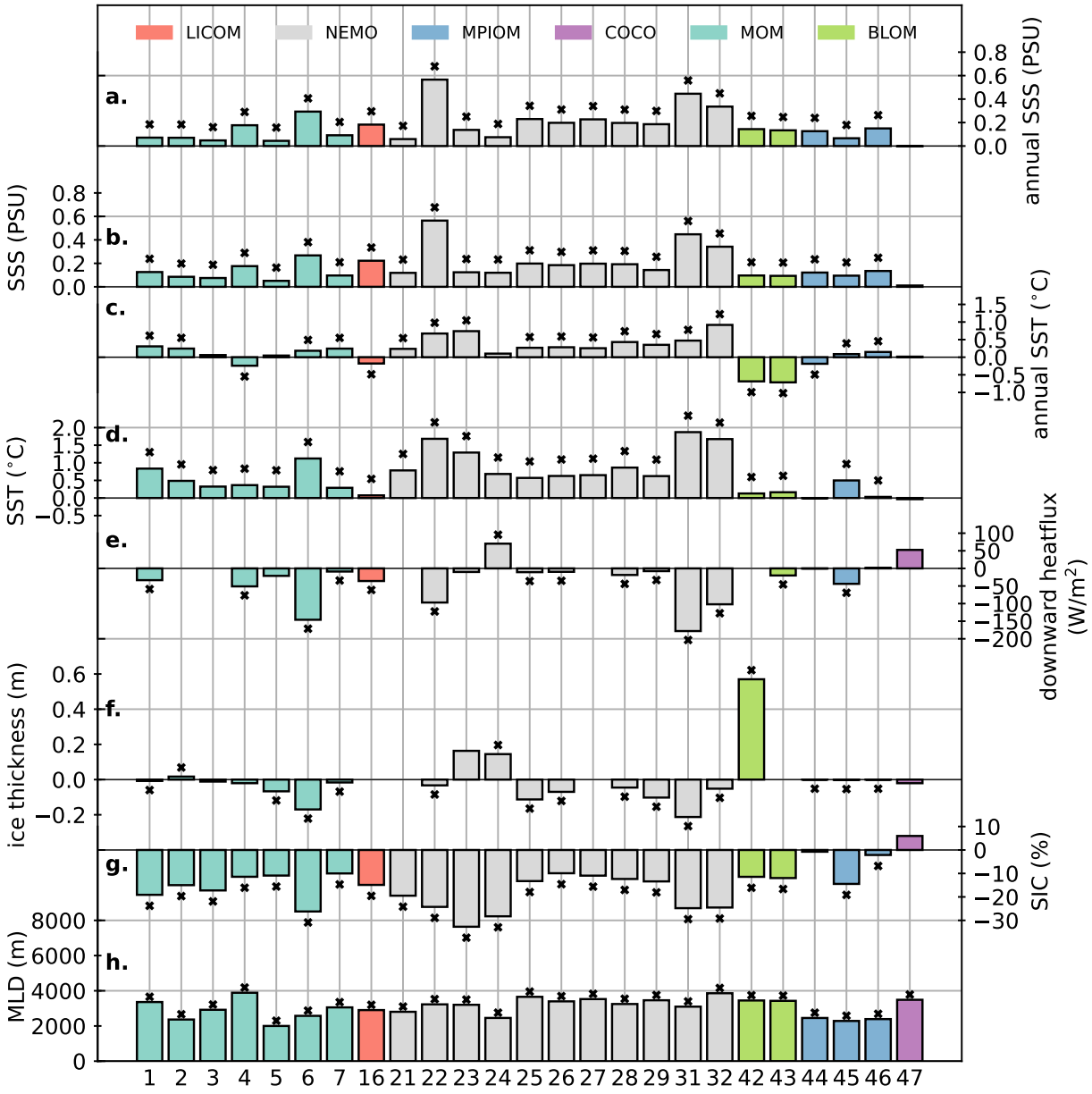

Figure 8. Differences in selected properties between deep and shallow OOP, calculated as deep minus shallow. Panels **a.–g.** show differences in: annual SSS, September SSS, annual SST, September SST, downward heat flux, ice thickness, SIC, and MLD. The "x" symbol on each bar indicates a statistically significant difference between deep and shallow OOP ($p < 0.005$).

https://doi.org/10.5194/egusphere-2026-3060
Preprint. Discussion started: 10 July 2026

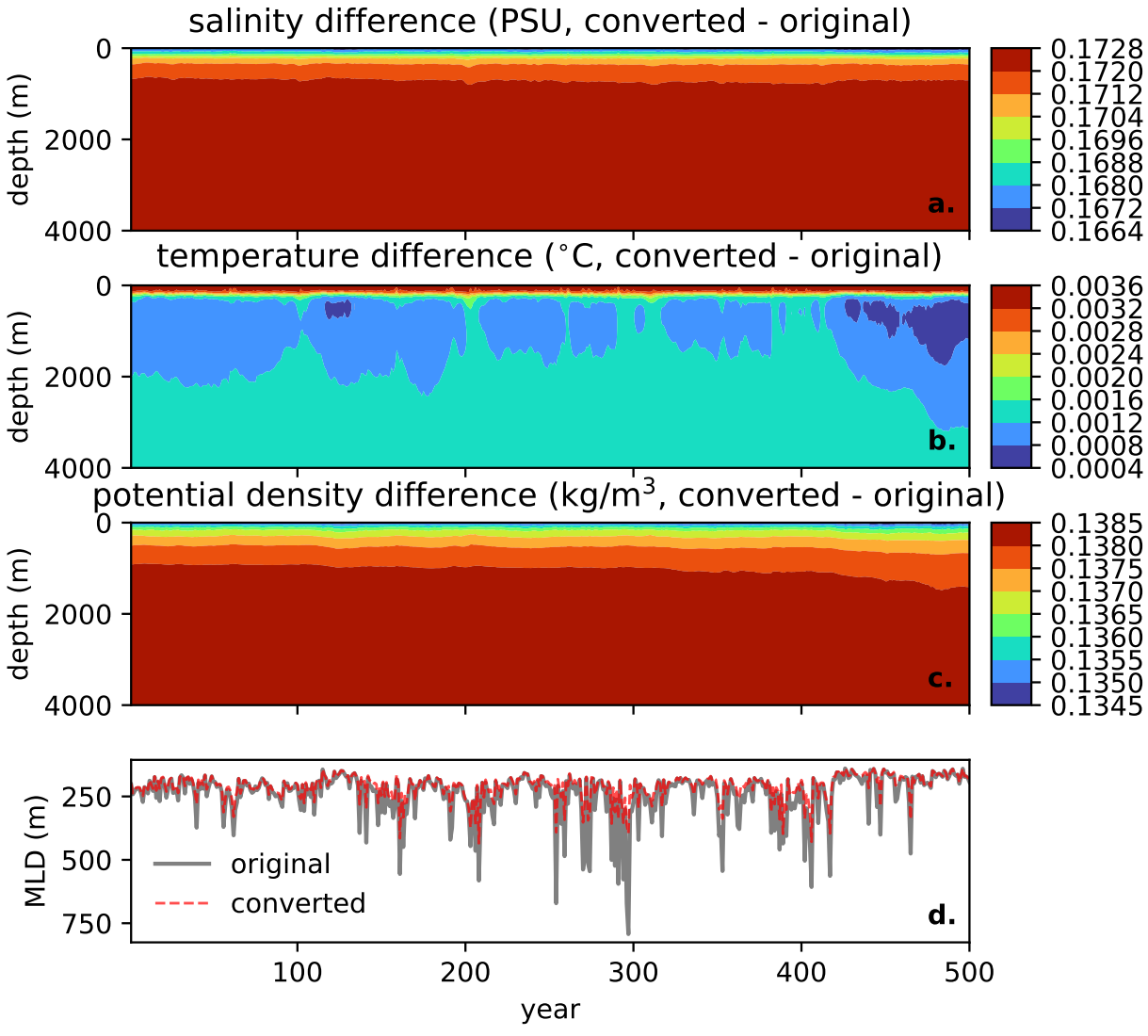

Figure A1. Differences observed after converting September model outputs of potential density ("thetao") and sea water salinity ("so") to conservative temperature and absolute salinity. Data are from the SO Weddell Sea region using the GFDL-CM4 model. Results are spatially averaged and presented as depth profiles over the entire simulation period. **a.** Difference between converted absolute salinity and the original model output "so". **b.** Difference between converted conservative temperature and and model original output "thetao". **c.** Difference in potential density calculated using converted variables (conservative temperature and absolute salinity) versus using model original outputs ("thetao" and "so"). **d.** Comparison of MLD detection based on potential density computed from converted variables versus that from original model variables.

https://doi.org/10.5194/egusphere-2026-3060
Preprint. Discussion started: 10 July 2026

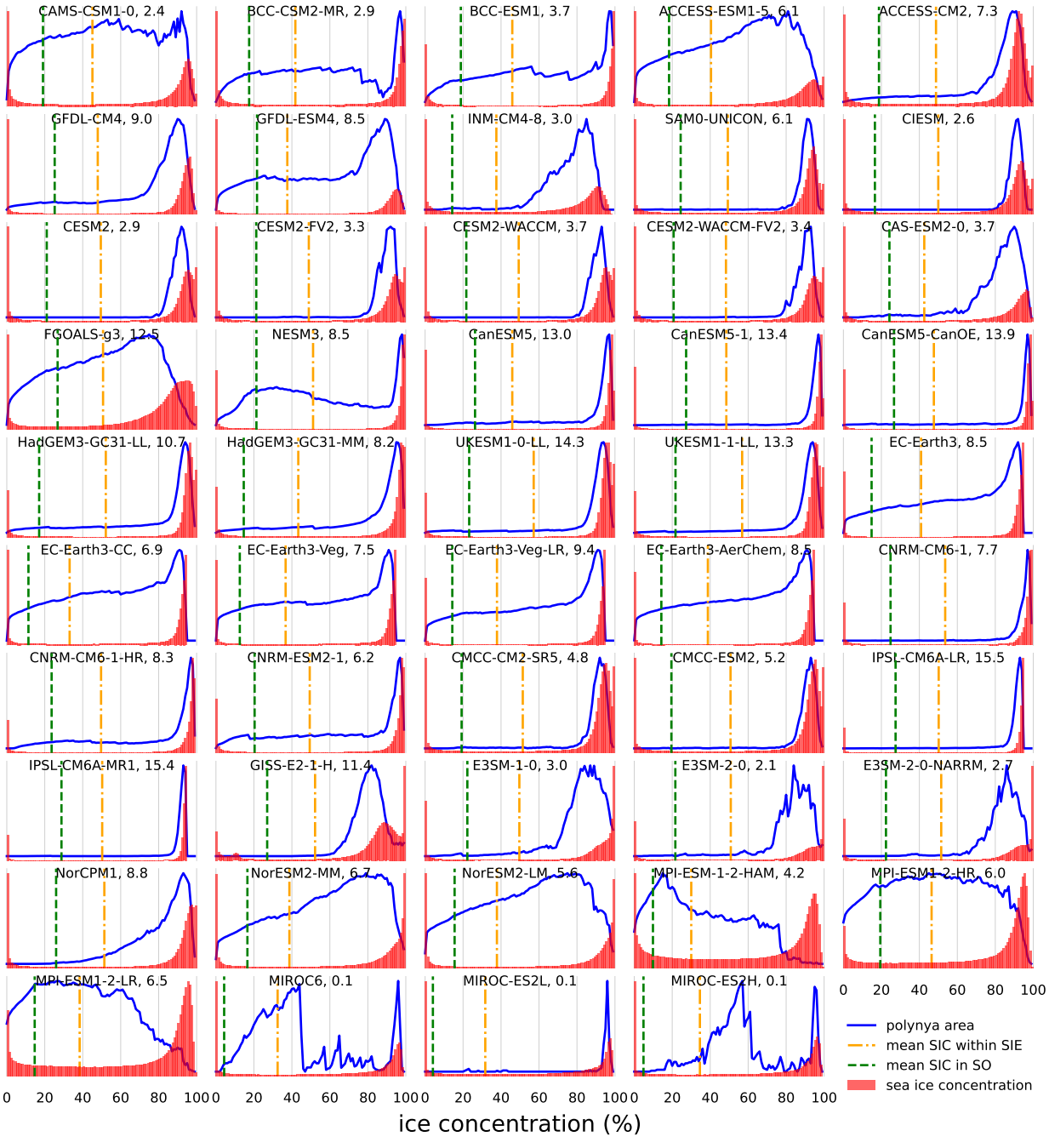

Figure B1. SIC characteristics and open polynya detection across climate models using varying criteria. The red histogram represents the distribution of SIC across the SO over study period. The blue continous line illustrates the total detected polynya area under different SIC threshold criteria, as identified by the x-axis. The orange line is the final threshold chosen across models for this paper. The vertical green line denotes the mean SIC (averaged over time and space) across the SO, while the vertical orange line shows the mean SIC within the sea ice extent (excluding grid cells with zero ice concentration, long-time averaged).For reference, each panel is labeled with the corresponding model name and with the maximum total open polynya area expressed in 10^9 km^2. OOPs are defined as regions of open water fully enclosed by sea ice, with no direct connection to the open ocean. No Cutoff used for polynya areas. Note that the y axis differs among models, and goes from 0 to the respective maximum area of the total OOP.

https://doi.org/10.5194/egusphere-2026-3060
Preprint. Discussion started: 10 July 2026

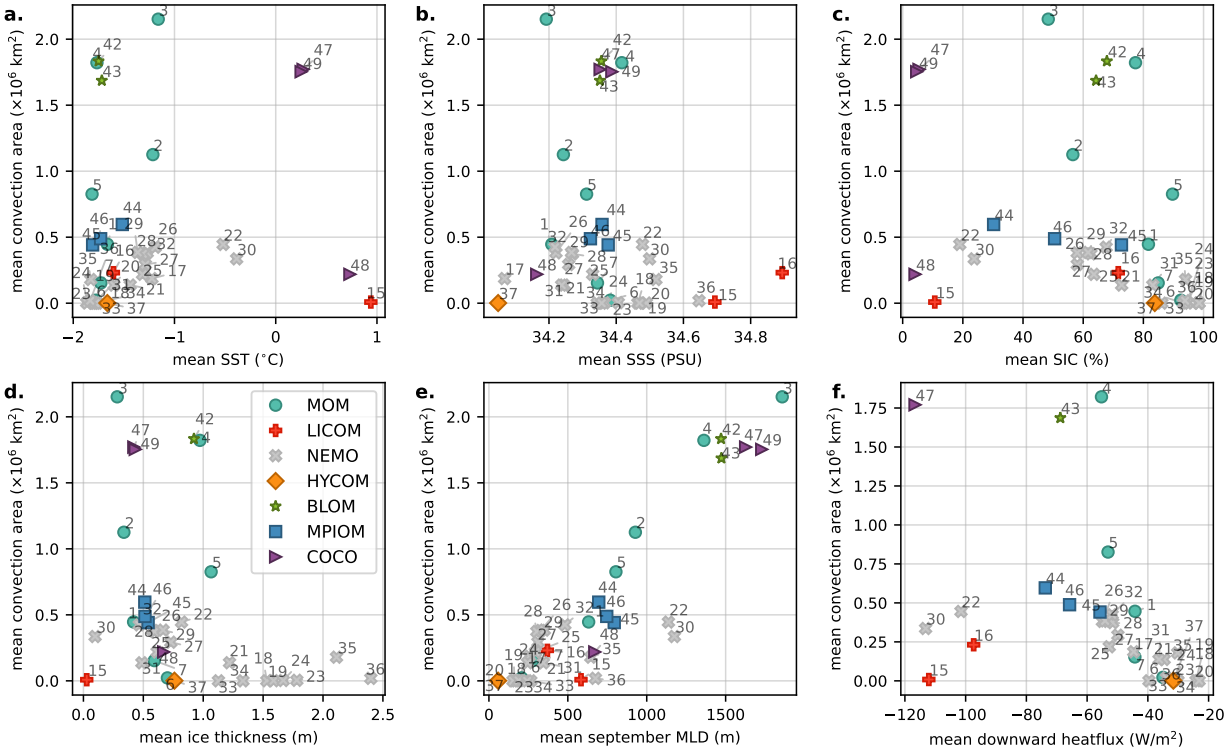

Figure C1. Dynamics within deep convection regions compared to the mean convective area. Each panel presents scatter plots of the mean properties inside deep convection regions for: **a.** mean SST, **b.** mean SSS, **c.** mean SIC, **d.** mean ice thickness, **e.** mean MLD, and **f.** mean downward surface heat flux.

https://doi.org/10.5194/egusphere-2026-3060
Preprint. Discussion started: 10 July 2026

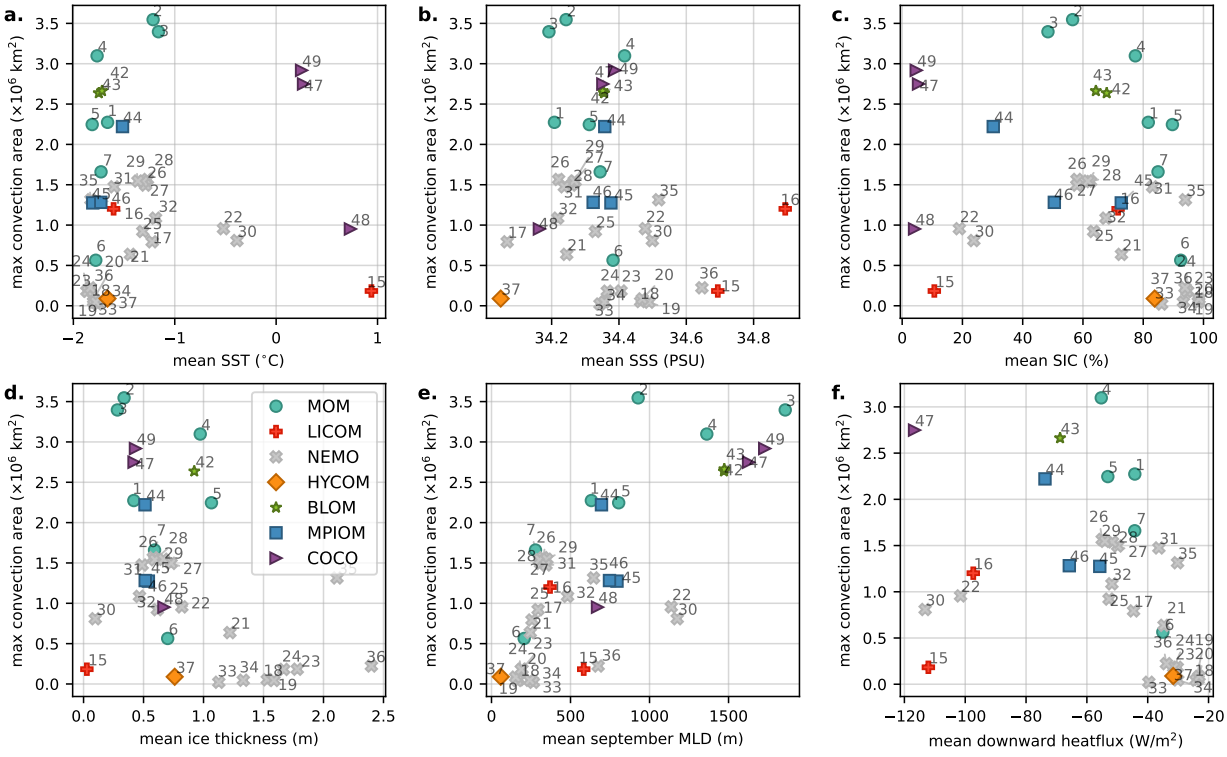

Figure C2. Dynamics within deep convection regions compared to the max convective area. Each panel presents scatter plots of the mean properties inside deep convection regions for: **a.** mean SST, **b.** mean SSS, **c.** mean SIC, **d.** mean ice thickness, **e.** mean MLD, and **f.** mean downward surface heat flux.

https://doi.org/10.5194/egusphere-2026-3060
Preprint. Discussion started: 10 July 2026

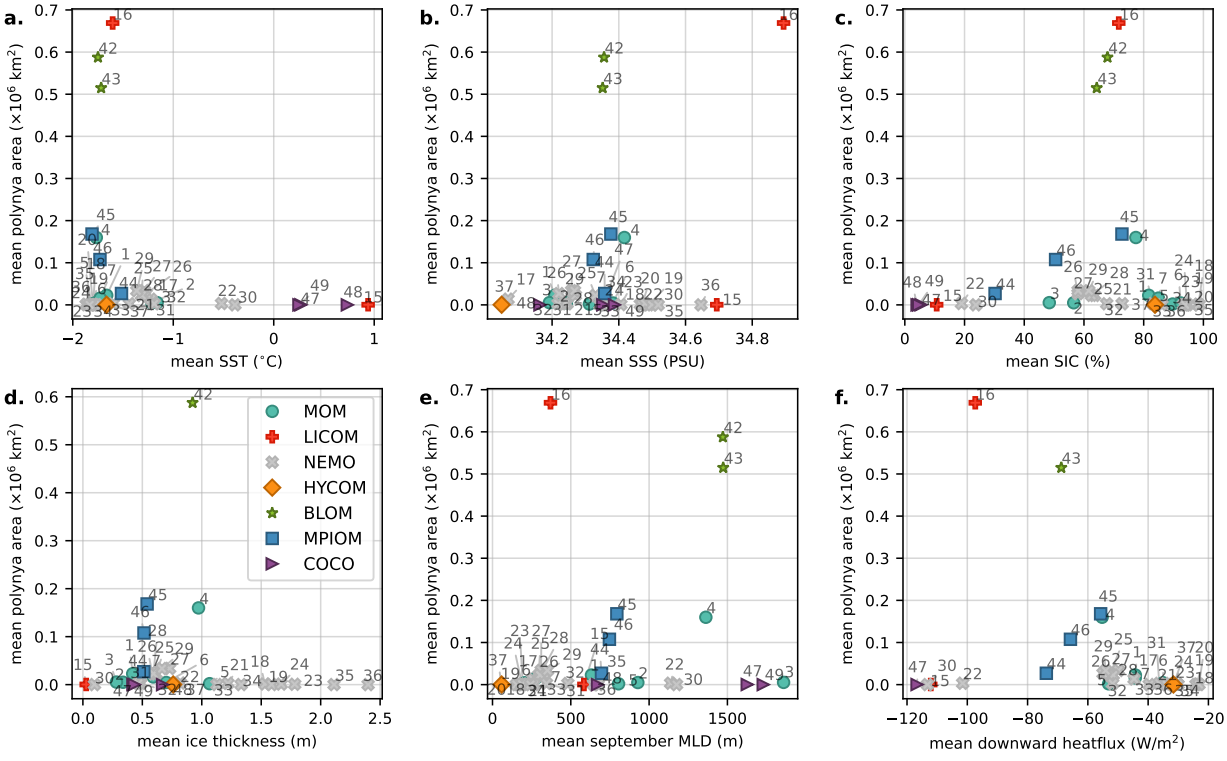

Figure C3. Dynamics within OOP regions compared to the mean OOP area. Each panel presents scatter plots of the mean properties inside OOP regions for: **a.** mean SST, **b.** mean SSS, **c.** mean SIC, **d.** mean ice thickness, **e.** mean MLD, and **f.** mean downward surface heat flux.

https://doi.org/10.5194/egusphere-2026-3060
Preprint. Discussion started: 10 July 2026

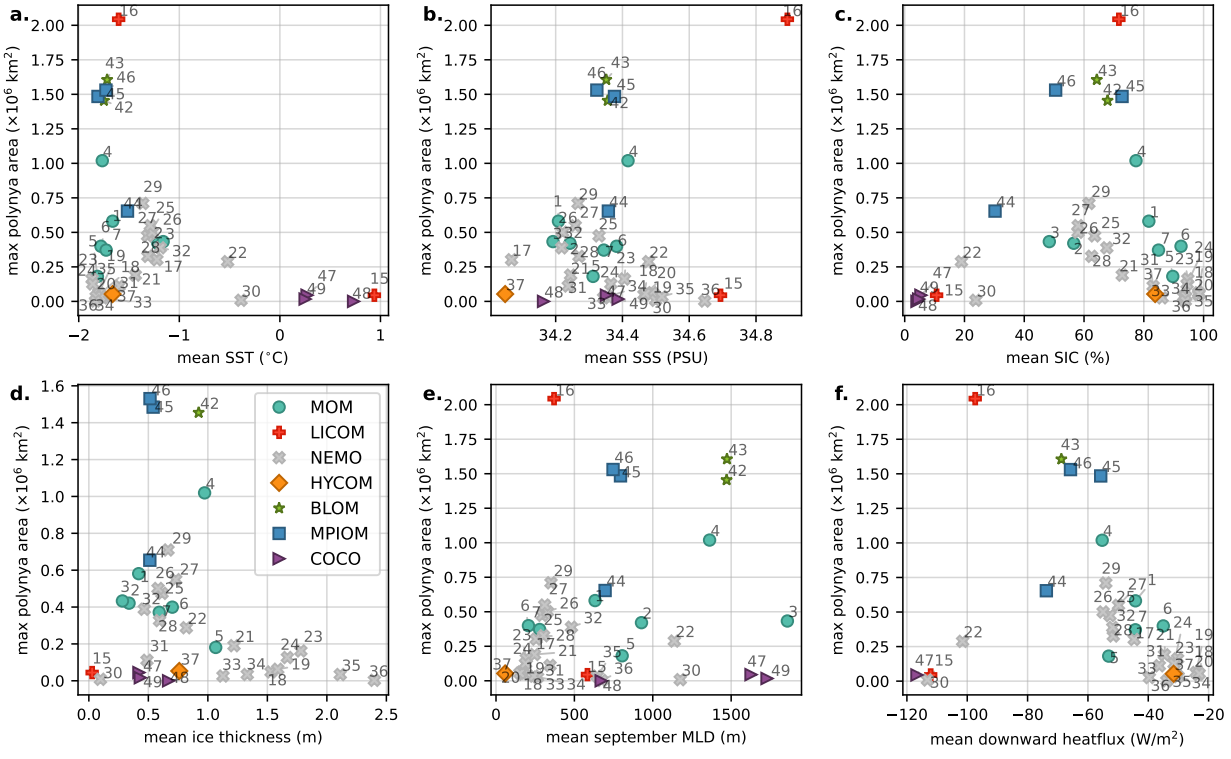

Figure C4. Dynamics within OOP regions compared to the max OOP area. Each panel presents scatter plots of the mean properties inside OOP regions for: **a.** mean SST, **b.** mean SSS, **c.** mean SIC, **d.** mean ice thickness, **e.** mean MLD, and **f.** mean downward surface heat flux.

https://doi.org/10.5194/egusphere-2026-3060
Preprint. Discussion started: 10 July 2026

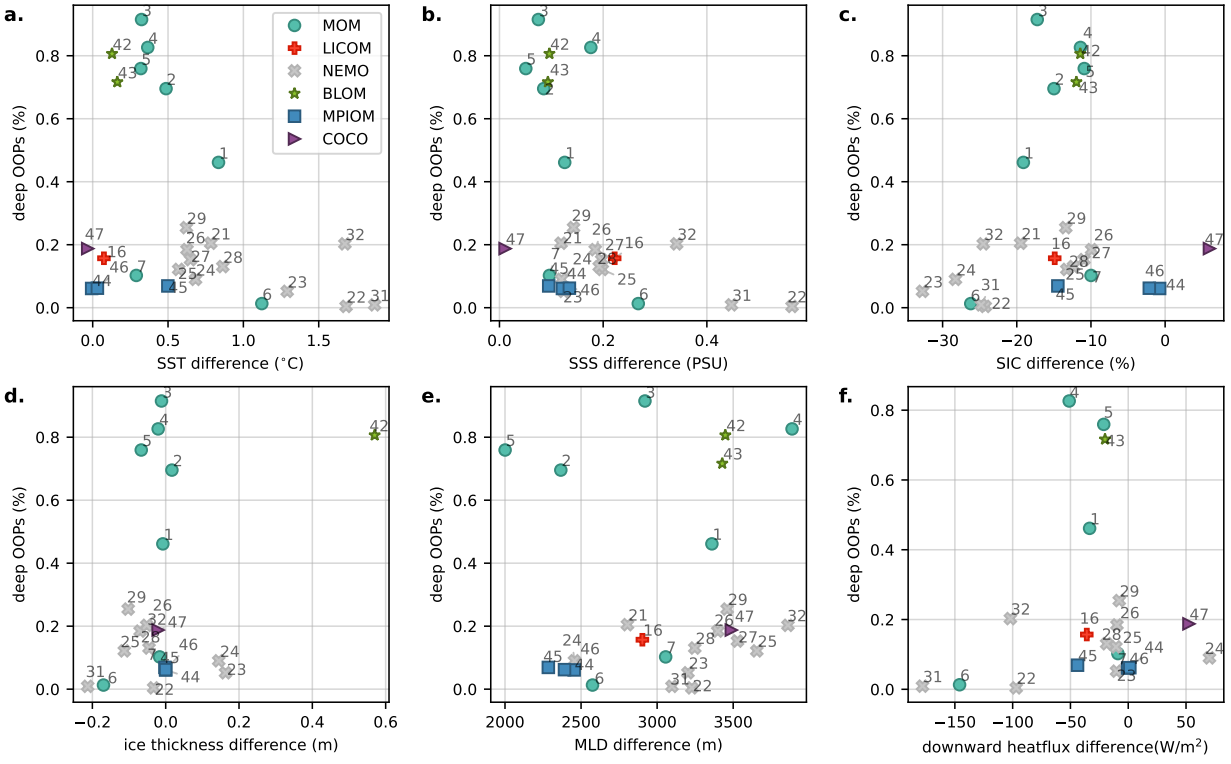

Figure C5. Differences in properties between deep and shallow OOP as a function of the percentage of deep OOPs among all detected OOPs. Each panel presents scatter plots of the differences inside deep versus shallow OOPs for: **a.** SST, **b.** SSS, **c.** SIC, **d.** ice thickness, **e.** MLD, and **f.** downward surface heat flux.